CHALMERS

Enhancing Shoulder Joint Biofidelity in the VIVA+ Human Body Model and Evaluating its Response

Bachelor's thesis in Mechanical Engineering

Rasmus Fyr
Mollie Martinsson
Lilas Qaddoura
Hannah Raab
Karin Svensson
Elin Åberg

DEPARTMENT OF MECHANICS AND MARITIME SCIENCES

CHALMERS UNIVERSITY OF TECHNOLOGY

Gothenburg, Sweden 2026

www.chalmers.se

Bachelor's Thesis in Mechanical Engineering

Enhancing Shoulder Joint Biofidelity in the VIVA+ Human Body Model and Evaluating its Response

Rasmus Fyr
Mollie Martinsson
Lilas Qaddoura
Hannah Raab
Karin Svensson
Elin Åberg

CHALMERS

Department of Mechanics and Maritime Sciences
Division of Vehicle Safety
Chalmers University of Technology
Gothenburg 2026

Enhancing Shoulder Joint Biofidelity in the VIVA+ Human Body Model and Evaluating its Response

Rasmus Fyr
Mollie Martinsson
Lilas Qaddoura
Hannah Raab
Karin Svensson
Elin Åberg

Supervisors: Shinya Abe, Chiara Rosanna Fichera, Jobin John. Department of Mechanics and Maritime Sciences, Division of Vehicle Safety.
Examiner: Johan Iraeus, Department of Mechanics and Maritime Sciences, Division of Vehicle Safety.

Bachelor's Thesis 2026
Department of Mechanics and Maritime Sciences
Chalmers University of Technology
SE-412 96 Gothenburg
Telephone +46 31 772 1000

Cover : VIVA+ human body model during simulation of lateral shoulder impact on the right shoulder from Compigne et al. (2004). Some soft tissues on the right side were removed for visual purposes only.

Typeset in LaTeX
Gothenburg 2026

Enhancing Shoulder Joint Biofidelity in the VIVA+ Human Body Model and Evaluating its Response

Rasmus Fyr, Mollie Martinsson, Lilas Qaddoura,
Hannah Raab, Karin Svensson, Elin Åberg
Department of Mechanics and Maritime Sciences
Division of Vechicle Safety
Chalmers University of Technology

Abstract

Previous versions of the VIVA+ human body models have demonstrated excessive shoulder stiffness compared to experiments conducted on postmortem human subjects. This study aims to enhance the biofidelity of the shoulder in the VIVA+ model. Data from studies involving postmortem human subject experiments were extracted and applied to two separate models of the acromioclavicular and sternoclavicular joint. Different verification tests were implemented to ensure that the mechanical properties of the joints were implemented correctly. The data from the studies were also used to construct biomechanical response corridors. The model modifications were implemented and evaluated in LS-DYNA, and the corridors were constructed in Python using principal component analysis and Bayesian regression. Initially, a force-deflection corridor was intended, but limitations in the deflection data restricted the final corridor construction to the force-time response. Analysis of the corridors showed that the choice of principal components affected the physical reasonability. The final validation of the updated model involved comparing it with the previous iteration and the response corridors. By implementing the joints in an updated model in LS-DYNA and comparing the simulated VIVA+ response with these corridors, it was possible to assess how closely the updated model was to the experimental human response. The results showed that the updated model was less stiff than the original VIVA+ model, for all model types. The comparison to the corridors showed that the modified model was closer to the corridors at lower impact speed, while the response at higher speeds still differed from the experimental range. This indicates that the updated shoulder joints improved the response of the model, but further development is still needed to fully represent the biomechanical behaviour of the shoulder.

Keywords: Bayesian Regression, Finite Element Method, Human Body Model, Principle Component Analysis, Shoulder Joint

Acknowledgements

We would like to thank our supervisors Chiara Rosanna Fichera, Shinya Abe and Jobin John for their guidance and support throughout this project. We truly appreciate our project and questions being prioritised even when it has been during evenings and weekends. It has been inspiring to gain insight in what the Vehicle Safety division does, and to be a part of developing something meaningful.

We would also like to thank our examiner, Johan Iraeus, for providing this project, as well as teaching us the basics of human body models.

Rasmus, Mollie, Lilas, Hannah, Karin & Elin,
Gothenburg, May, 2026

Acronyms

All acronyms used in this thesis are listed below in alphabetical order:

AC	Acromioclavicular
AP	Anterior-Posterior
ATD	Anthropomorphic Test Device
CA	Coracoacromial
CC	Coracoclavicular
DOF	Degree of Freedom
ELPD	Expected Log Pointwise Predictive Density
FE	Finite Element
FEM	Finite Element Method
HBM	Human Body Model
HDI	Highest Density Interval
LOO	Leave-One-Out
ML	Medial-Lateral
NUTS	No-U-Turn Sampler
PC	Principal Component
PCA	Principal Component Analysis
PMHS	Postmortem Human Subjects
RMSE	Root Mean Square Error
SC	Sternoclavicular
SI	Superior-Inferior

Contents

1

Introduction

1.1 Background

Road traffic injury is the leading cause of death for children and young people aged 5 to 29 years. It is also the 12th leading cause of death when all ages are considered (World Health Organization, 2023). The Vision Zero initiative was first implemented in Sweden in 1997 and has now spread globally. It is a concept aimed at preventing anyone from dying or being seriously injured in a road accident. According to Vision Zero, the main problem is not that accidents occur, but that many of them lead to death or lifelong impairment. So instead of trying to prevent them, the idea is to find solutions and change the traffic system so that accidents will not have serious consequences (Swedish Environmental Research Institute, n.d.). The number of deaths and injuries related to vehicles can be reduced by improving today's crash safety systems and using more biofidelic subjects, this can be done with human body models (HBMs).

1.1.1 Human Body Models

Finite element (FE) HBMs are used to simulate and study how the human body responds to external loads, typically in motor vehicle collisions (Fahse et al., 2023). There is a need for a model of the human body since testing for severe injuries cannot be done on living human beings (Iraeus, 2026). HBMs are used in both academic research and industrial applications to support the development of safer vehicles and reduce the risk of personal injury (Fahse et al., 2023).

Today, the most accurate models for representing human responses in testing are post-mortem human subjects (PMHS) and the results from these PMHS tests are what all other HBM results are compared to. Testing only with PMHS would mean that injuries requiring a physiological response could not be quantified. PMHS that meet the desired criteria for age, gender, etc., are also difficult and costly to obtain (Beeman et al., 2012). Because of this physical crash test dummies, or anthropomorphic test devices (ATDs), are used. These are validated against PMHS before use. ATDs are designed to be used repetitively and to show the same response across tests. Although the responses of these devices

are not validated for alternate loading conditions and thus may not produce biofidelic responses beyond their intended design specifications (Beeman et al., 2012). In addition, ATDs are expensive and require a physical car for testing, limiting the number of tests that are reasonable to perform (Fahse et al., 2023; Toyota Motor Corporation, 2021). ATDs later evolved into virtual models of crash test dummies and further into virtual HBMs of actual human bodies (Iraeus, 2026). All of these model types can be used for vehicle safety testing, but the FE-HBMs have advantages. Unlike testing with ATDs, simulations of HBMs can be used to investigate organ-level injuries (Devane et al., 2023).

1.1.2 Applications and Benefits of Biofidelic Models

FE-HBMs and ATDs have different strengths and work best when complemented with each other. Below, different cases are listed and explained how they benefit from being modelled with an FE-HBM.

With FE-HBMs, it is possible to analyse the body throughout different phases of crashes (Fahse et al., 2023). In the case study presented in the article by Fahse et al. (2023), an HBM has been positioned on a motorcycle and a crash simulation has been made. The trajectories of chosen areas on the human body have been traced throughout the crash. This allows for a more detailed analysis of the different phases of a crash and help us better understand how injuries happen. This can also be done using ATDs, but by using FE-HBMs each scenario require less resources.

It is difficult to properly position ATDs on micromobility vehicles because they must be secured in place. As a result, their response is not biofidelically representative in this position, which limits their applicability (John et al., 2022). Therefore, there are many situations where these ATDs are not suitable, such as pedestrians, cyclists, and e-scooter riders in traffic. To represent these types of situations, it is advantageous to use the FE-HBM (John et al., 2022).

Current ATDs, such as Hybrid III and THOR, have a limited ability to represent real shoulder-belt interactions. This could be seen in crash simulations when the seat belt slips off at high angles when no pretensioner is used, which occurs because the model is too rigid and the seatbelt does not sink in. A more biofidelic shoulder joint could help better represent how a real human shoulder interacts with the seat belt and improve the prediction of belt slippage, especially in oblique impacts (Douglas et al., 2007). The Hybrid III ATD does not have any load sensors in the shoulder itself, only one main on the chest. During a real crash, up to half of the shoulder belt load can be applied to the shoulder region. Due to the lack of sensors, the Hybrid III essentially overlooks that path.

This gives an inaccurate representation of the seatbelt load distribution in real life crashes and can lead to uncertainties in shoulder injury risk and difficulty in evaluating seatbelt and airbag designs. Implementing a more biofidelic shoulder joint model would reduce uncertainty in injury prediction and allow a more reliable evaluation of seatbelt and airbag performance (Douglas et al., 2007).

There are many fields where FE-HBMs can be used, a few examples of applications in traffic safety and their benefits are explained above. These examples show that the establishment of a more biofidelic joint would support further improvement of safety measures.

1.2 Aim

The aim of this project is to improve shoulder biofidelity in the VIVA+ HBM by refining the acromioclavicular (AC) and sternoclavicular (SC) joint properties, and evaluating it against existing PMHS data. In addition to this, the project also includes the construction of biomechanical response corridors from experimental data. Different construction methods will be compared in order to identify the most well described corridors.

1.3 Scope Restrictions

The project is subject to several limitations that were taken into account when interpreting the results.

- The VIVA+ model is implemented solely within LS-DYNA and is not extended to other FE software.
- Simplified versions of the different types of joints are implemented in the model. In this thesis only joint properties were modelled, no other anatomical components such as muscles, cartilages or joint capsule are modelled.
- No physical tests are conducted within the scope of this work. The project relies on data from previous published experiments on PMHS.
- The experimental data used for validation are based on previous experiments on PMHS. Therefore, it cannot be assumed that the results fully represent the response of living human beings, as the test subjects are unable to react to the impact or perform any bracing actions.

1.4 Ethical Aspects

Data from previous biomechanical experiments are used in the project. This means that there are no direct ethical issues for test subjects, but it is important to interpret the results correctly and responsibly.

A potential risk could be if the model is used outside its validated range. Since the model is built for specific conditions, it may not be biomechanically representative for other scenarios. This could lead to false injury predictions, and constructions based on the model could be evaluated as safe even though they are not.

However, there are possible positive effects of the result. By developing simulated HBMs, the need for physical tests is reduced. This is positive in an economic perspective, since the physical tests are expensive (Iraeus, 2026). But also in an societal perspective, since simulated HBMs allow for development of a wider range of conditions. This could, in the long term, lead to a reduced risk of injury.

2

Theory

2.1 Shoulder Anatomy

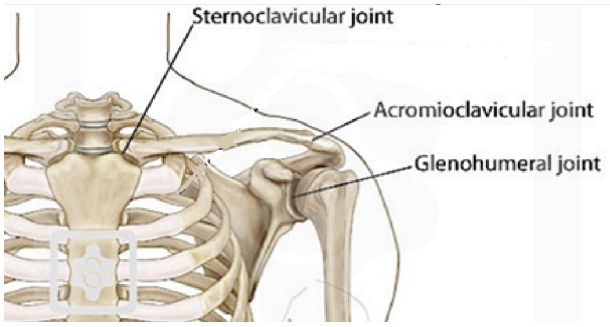

Figure 2.1: Joints of the shoulder. Adapted from (Avani, 2024) CC-BY-4.0

The shoulder region (see Figure 2.1) is anatomically complex, consisting of several structures such as bones, joints, and ligaments that together allow a wide range of motion. The biomechanical behaviour of the shoulder significantly influences the motion of the upper body and the distribution of the load during a crash. Due to this complexity, the shoulder is also challenging to model, making it a particularly interesting anatomical region.

One of the main components of the shoulder is the clavicle, which is positioned horizontally between the sternum and the scapula (Hills-Meyer & Stamm, 2019). The clavicle consists of three regions, a medial (sternal) end that articulates with the sternum, a lateral (acromial) end that articulates with the scapula, and a shaft between the two ends. The clavicle serves as an attachment for several muscles and contributes to the range of motion of the glenohumeral joint, allowing movement of the arm in three dimensions. The scapula is located posteriorly to the clavicle (Hills-Meyer & Stamm, 2019). It is a flat, triangular bone with a lateral, superior, and inferior border (Drake et al., 2015). The articulation between the clavicle and scapula occurs at the acromion, which is a bony process located on the superior lateral part of the scapula (Hills-Meyer & Stamm, 2019) - together forming the AC joint. The sternum connects to the medial end of the clavicle, forming the SC joint. Another process, called the coracoid process, is positioned anteriorly on the superior lateral part of the scapula (Drake et al., 2015). Between the acromion and the coracoid process

lies the glenoid cavity, which articulates with the humerus. The proximal end (humeral head) articulates with the scapula at the glenoid cavity, forming the glenohumeral joint (Hills-Meyer & Stamm, 2019).

2.1.1 Anatomical Map

When describing the human body, an anatomical position of the body is used as a standard reference (Hills-Meyer & Stamm, 2019). This is when the body is in a standing upright position, with the palms of the hands forward. To be able to describe structures relative to each other in the human body, directional terms are used. Common terms that are used are: anterior-posterior (AP), superior-inferior (SI), medial-lateral (ML), and proximal-distal. These expressions are used to describe the direction of body parts relative to each other. AP describes a part in front of or behind another part of the body. SI describes a part above or below another part of the body. ML describes a part closer to the centre or the side of the body. Proximal-distal describes a part nearer or farther from the other part (Hills-Meyer & Stamm, 2019).

2.1.2 Acromioclavicular Joint

The AC joint is a plane synovial joint between the clavicle and the acromion of the scapula. It allows limited movement in the AP and SI directions, as well as small axial rotation (Hills-Meyer & Stamm, 2019). The movements in the joint are affected by a joint capsule and several ligaments: the AC, the coracoclavicular (CC), and the coracoacromial (CA) ligament. The AC ligaments include a superior, inferior, anterior, and posterior part, where the superior ligament is the most important for stabilisation of the joint. The CA and the CC ligaments - i.e. trapezoid and conoid ligaments - contribute to vertical stability (Kiel et al., 2022).

2.1.3 Sternoclavicular Joint

The SC joint connects the medial end of the clavicle to the sternum (Hills-Meyer & Stamm, 2019). It is a saddle synovial joint that allows translation along three axes, AP, SI, and limited rotation of the clavicle (Drake et al., 2015). The joint is stabilised by the anterior SC ligament which restricts displacement in the superior direction. The posterior capsular ligament which provides stability in the AP direction. The interclavicular ligament provides medial traction between the clavicles. The costoclavicular ligament provides stability between the clavicle and the anterior first rib (Kiel et al., 2023).

2.2 Finite Element Method

Finite Element Method (FEM) is a numerical method that can be used to solve problems governed by differential equations that do not have analytical solutions (Balderes, 2026).

The geometry is discretised into smaller regions called finite elements, collectively forming a mesh, where shape functions are used to approximate the solution for each element. Together, these functions form an approximation of the solution for the geometry in full. This is beneficial for complicated geometries, or geometries where the material properties change throughout the domain (Reddy, 2019). FEM is often used to determine deformation or displacement of a structure due to external loads (Morita, 2021).

2.2.1 Material Properties

In this section, the different mechanical properties used for modelling the shoulder joints are presented.

2.2.1.1 Young's Modulus

Young's modulus is a parameter that describes the ratio between the change in stress and the change in strain in the elastic region of a material. The value can differ for tensile and compressive stress (Krefeld & Bowman, 2020). Young's modulus can be calculated from a stress-strain curve by calculating the slope of the graph in the linear-elastic area

$$E = \frac{\Delta\sigma}{\Delta\varepsilon}, \tag{2.1}$$

where σ is stress and ε is the strain (Krefeld & Bowman, 2020).

2.2.1.2 Poisson's Ratio

Poisson's ratio describes how a material deforms in lateral and axial direction while being stretched or compressed (ScienceFacts, 2025). It can be calculated by taking the negative value of the lateral strain divided by the longitudinal strain (The Engineering ToolBox, 2008). Because most materials compress sideways, a negative sign is added so that Poisson's ratio remains positive. A negative Poisson's ratio value means that the material will expand equally in the lateral and longitudinal directions while being stretched.

2.2.1.3 Elastic Stiffness

Elastic stiffness, K, describes the ratio of the load to displacement, which explains how the structure resists deformation. A lower stiffness indicates a softer and a less stiff structure, while a high is the opposite (Barczak, 2017). The elastic stiffness for a discrete element is calculated with the formula

$$K = \frac{F}{\delta}, \tag{2.2}$$

where F is the force applied and δ is the displacement of the element.

2.2.1.4 Yield Stress

The yield stress is the point on the stress-strain curve where the elastic region ends and the plastic region begins. At this stress level the material deforms plastically (Engineering Technology, 2026).

2.2.2 LS-DYNA

LS-DYNA is an FE-solver for dynamic simulations, with the possibility of solving fluid, electromagnetic, and structural problems. It has different elements and over 300 different material models that can be used to model different structures (Ansys Inc, 2023).

2.2.2.1 Discrete Spring Elements and Discrete Beam Elements

In LS-DYNA several different elements can be used. Two common ones two common ones to represent a 1-D spring type structure are the discrete spring and the discrete beam element. The discrete spring is an element that has one degree of freedom (DOF), hence it can only take axial forces. The discrete beam element has six DOFs, and can be seen as six combined discrete elements, one for each DOF (DYNAmore GmbH, 2026).

2.2.2.2 Material Cards

Elements in LS-DYNA need to be assigned a material card. Different combinations of material cards and element types will result in different results when simulating. The different material cards require different input parameters and can provide different levels of detailed properties.

The material card *Spring Elastic* and the material card *Spring Nonlinear Elastic* are two of the simplest material cards that can be used for discrete springs and dampers. The first requires the elastic stiffness, K, as input whereas the latter requires a force-displacement curve or moment-rotation curve. Therefore *Spring Elastic* can only provide linear elastic properties, while the *Spring Nonlinear Elastic* card can provide more advanced, e.g. non-linear, curves (Livermore Software Technology, 2020).

For discrete beams, some of the simpler material cards are *Elastic* and *Plastic Kinematic*. These require density, Young's modulus and Poisson's ratio. For *Plastic Kinematic*, yield stress and tangent modulus is also required (Livermore Software Technology, 2020). Since the yield stress and tangent modulus (the slope of the stress-strain curve at a specific point) are included, it is possible to model a bilinear curve, and hence model slightly more complicated behaviour by modelling both the elastic and plastic response.

General Nonlinear 6 DOF Discrete Beam requires density and six different load curves for three translational and three rotational DOFs as input. The load curves are either

force-displacement curves, or moment-rotation curves, explaining the elements mechanical behaviour due to external loading. It is also possible to apply different properties for loading and unloading. This material card can model nonlinear material behaviour and can therefore model complex responses and have different behaviour in all six DOFs.

2.3 VIVA+ Model

VIVA+ is an open source set of FE-HBMs that is developed with a female average as the baseline (Iraues et al., 2025). The shoulder joints are modelled as spherical robotic joints, which is a simplification of the true joints. This joint only allows for rotation but no translation. Currently, in validated shoulder impact, the results for the shoulder response in load-deflection is stiffer compared to the PMHS tests and indicate that it is not biofidelic (John et al., 2022).

2.4 Biomechanical Response Corridors

Biomechanical response corridors describe the expected range of human mechanical responses during a specific loading condition, such as an impact. They are usually created from experimental data, for example, from PMHS, and show an upper and lower boundary around a group of measured response curves. These corridors can be used as a reference when evaluating ATDs or HBMs. If the observed response falls within the corridor, it indicates that the model gives a response that is close to the experimental human response. Biomechanical corridors are therefore useful for assessing the biofidelity of a model and for evaluating how well the simulated response represents experimental human response data (Sun et al., 2016).

2.4.1 Principal Component Analysis

Principal component analysis (PCA) is a method that makes complex datasets easier to work with by reducing the number of variables, while keeping as much important information as possible. This is useful when the dataset is large or difficult to interpret directly. In PCA, the original variables are reorganised into new components that represent the main patterns in the data. The first principal component (PC) describes the direction with the largest variation in the data, while the following components describe as much of the remaining variation as possible. The components are also uncorrelated with each other, which means that they describe independent modes of variation within the dataset (Jolliffe & Cadima, 2016).

In mathematical terms, PCA is based on finding eigenvectors and eigenvalues from the data. The eigenvectors describe the directions of the PCs, while the eigenvalues describe how

much variation each component explains. The amount of explained variance can therefore be used to decide how much variance should be retained when reducing the dimensions. If the first few PCs explain a large part of the total variation, the dataset can be represented in a lower-dimensional form without losing too much information (Jolliffe & Cadima, 2016).

In the context of biomechanical response corridors, PCA can be used to describe the main variation between several response curves. Instead of comparing every point of each curve separately, the curves can be represented by a smaller number of PC scores. These scores describe the most important differences between the curves, such as differences in magnitude or shape. This makes it easier to analyse the variation in experimental data and to later reconstruct representative response curves for corridor development (Jolliffe & Cadima, 2016).

2.4.2 Bayesian Inference

Bayesian inference handles unknown parameters as probability distributions instead of one single value. It is based on Bayes' Theorem, which updates prior knowledge about an unknown parameter θ using observed data

$$p(\theta|\text{data}) = \frac{p(\theta)p(\text{data}|\theta)}{p(\text{data})} \propto p(\theta)p(\text{data}|\theta). \tag{2.3}$$

The *prior* distribution $p(\theta)$ represents the probability of the parameter before the observed data and the *likelihood* $p(\text{data}|\theta)$ describes the conditional probability of the data given the parameter. These two combined results in the *posterior* distribution $p(\theta|\text{data})$, which is the updated distribution of the parameter after the observed data have been taken into account (Insua et al., 2012).

2.4.2.1 Posterior Sampling

For complex models, the posterior distribution is hard to compute analytically. Instead, it can be approximated numerically by generating a finite number of samples that represent the posterior distribution. One way to obtain these samples is by using Markov chain Monte Carlo (MCMC) methods. MCMC generates a sequence of random samples, where each draw depends on the previous one, and the procedure is constructed so that the distribution of all the samples converges towards the posterior distribution (Gelman et al., 2013).

Simulations of MCMC can be slow, due to the random walk through the target distribution. A solution to this is the MCMC method called Hamiltonian Monte Carlo (HMC), which removes the randomness by adding information about the posterior's slope at each step.

This results in a more efficient walk, since the HMC can move towards higher posterior probability and therefore converge faster (Gelman et al., 2013).

However, the HMC requires the user to decide the number of steps. If the number of steps is too small, the algorithm behaves like a random walk, moving inefficiently. If the number of steps is too large, the algorithm can turn back to where it came from, and that wastes computation time. An extension of the HMC is the No-U-Turn Sampler (NUTS), which automatically stops the algorithm when it starts to move back. This removes the decision about the number of steps, resulting in a more efficient algorithm (Hoffman & Gelman, 2014).

2.4.2.2 Model evaluation

After fitting a Bayesian model, an evaluation of the samples has to be done to ensure that the model is reasonable before interpreting the posterior distribution. This evaluation includes $\hat{R}$ statistics and divergences.

$\hat{R}$ compares the independent MCMC chains and computes the variance within and between them. This is used to evaluate whether the chains have converged towards the same distribution, where values close to one indicate that they have converged well. Divergences evaluate the inner workings of NUTS by reporting if there were any numerical problems with the sampling. A high number of divergences indicates that a region cannot be appropriately explored (Martin et al., 2024).

The predictive performance of different models can be compared using leave-one-out cross-validation (LOO), which estimates how well the model predicts unseen observations by repeatedly leaving one observation out and evaluating the model without that observation. Re-running the model every time a new observation is left out can be computationally expensive, therefore it can be approximated using the Pareto smooth importance sampling LOO. It calculates the expected log pointwise predictive density (ELPD), which measures the predictive accuracy. A higher ELPD indicates better expected predictive performance. The differences between the highest ranked model and the other models, together with their standard error, are given to determine if the rankings have a meaningful difference. Pareto-k values are used to evaluate the reliability of the LOO approximation. Each observation gets a Pareto-k value, with larger values indicating that the observation is influential, making the approximation less reliable (Martin et al., 2024).

2.4.3 Linear Regression

Linear regression is used to estimate the linear relationship between a response variable Y and one or more predictors X. The response variable is expressed as a linear function

$$Y = \beta_0 + \beta_1 X_1 + \beta_2 X_2 + ... + \epsilon, \tag{2.4}$$

where you can calculate the regression coefficients β_i and the residual ϵ using the values of Y and X (Bergh et al., 2021).

2.4.3.1 Bayesian Regression

Bayesian regression applies the Bayesian framework to regression models by handling the unknown parameters probabilistically and describing them as posterior distributions instead of just point estimates. The unknown parameters are assigned prior distributions that are then updated using observed data. This results in posterior distributions for the regression coefficients and residual. This approach provides both an estimate of the relationship between the response variable and the predictors, along with measures of the parameter uncertainties and the predictive uncertainty in this relationship (Bergh et al., 2021).

2.4.3.2 Multilevel Regression

Multilevel regression is a type of regression that is useful when the data are structured in different levels or groups. This means that some measurements are connected to each other. For example, several measurements can come from the same subject. In that case, the measurements from one subject may be more similar to each other than measurements from other subjects. Because of this, they should not always be treated as completely independent observations (Leyland AH, 2020).

A normal regression model often assumes that all observations are independent. If this assumption is not true, the model can give a misleading result. Multilevel regression handles this by taking the grouping in the data into account. It can separate variation between subjects from variation within the same subject (Leyland AH, 2020).

In a random intercept model, each subject can have its own starting level. This means that the model does not assume that all subjects have the same average response. The model still uses information from all subjects together, instead of treating every subject completely separately. This is useful when several response curves come from the same subject, because the model can include differences between subjects while still studying the general relationship between the variables and the principal component scores (Leyland AH, 2020).

3

Method

To achieve the project's aim a broad knowledge of the shoulder anatomy, mathematical concepts, and the modelling software was required. Therefore, a big part of the project involved gathering information through a literature review and video tutorials.

Based on that knowledge, the methods were chosen. To model both the AC and SC joints, the discrete beam together with the material card *General Nonlinear 6 DOF Discrete Beam* was implemented. For the corridor construction, PCA and Bayesian regression was used. Detailed implementation of both FE modelling and corridor construction is described in the upcoming sections.

3.1 Acromioclavicular Joint Implementation

In this section, the methods for implementation of the AC joint is described. The data used for implementation of the AC joint is from Dawson et al. (2009), Flores et al. (2023), Goodine et al. (2022), Koh et al. (2004), and Morikawa et al. (2020).

3.1.1 Placing of Ligament

The old robotic joint was removed. The beam was then placed between the lateral end of the clavicle and the acromion of the scapula, on their respective rigid parts. The rigid parts were created with the material card *Rigid* and were implemented to allow for the application of a loading rate on the model.

3.1.2 Coordinate System

The coordinate system was defined as in Goodine et al. (2022). The origin of the coordinate system was placed at the conoid ligament, on a node near the conoid tubercle. The x-axis was aligned with the clavicle. The y-axis was in the AP direction and the z-axis in the SI direction.

3.1.3 Load Curves

The material card *General Nonlinear 6 DOF Discrete Beam* requires six different load curves as input, namely three load curves for the translational DOF and three load curves for the rotational DOF. The load curves, see Figure 3.1, were obtained from several studies (Dawson et al., 2009; Flores et al., 2023; Goodine et al., 2022; Koh et al., 2004; Morikawa et al., 2020). In LS-DYNA the load curves are implemented with the units mm, ms, kN, and radians.

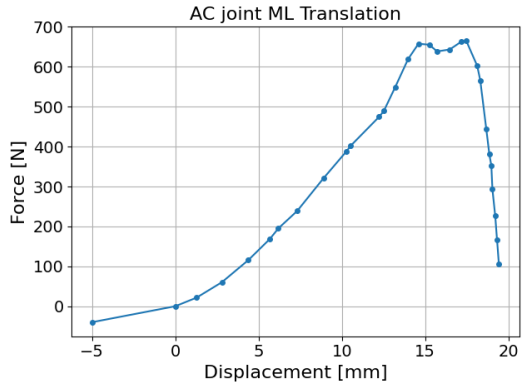

(a) ML Translation

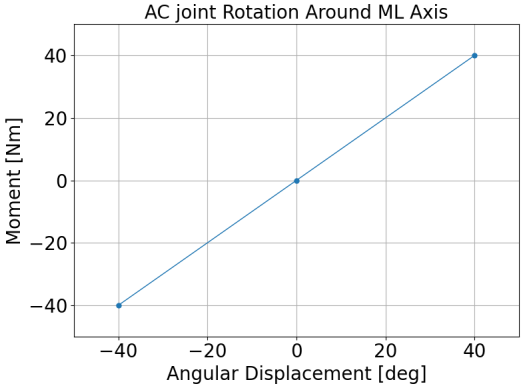

(b) ML Rotation

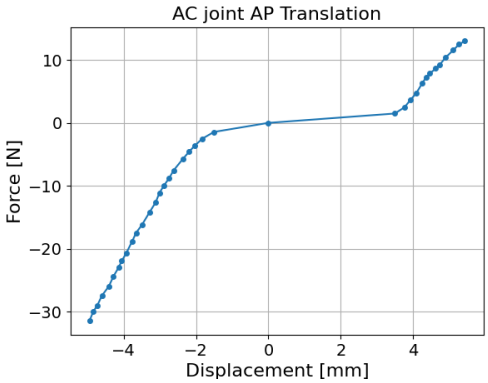

(c) AP Translation

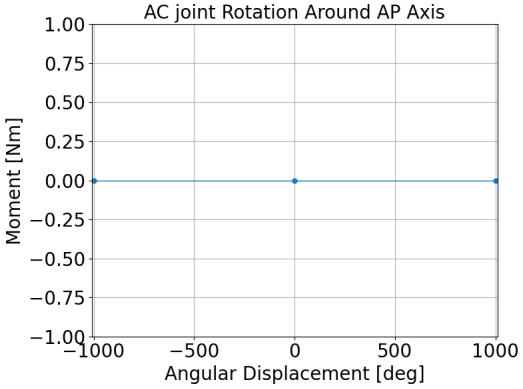

(d) AP Rotation

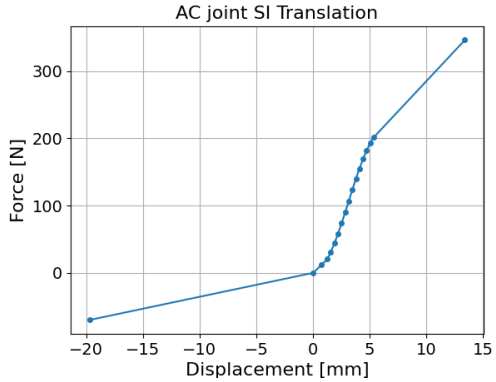

(e) SI Translation

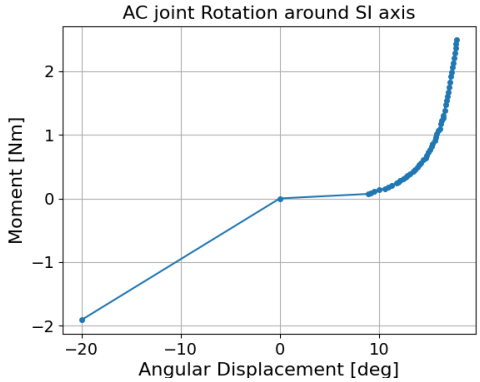

(f) SI Rotation

Figure 3.1: Translational and rotational loadcurves for AC joint.

3.1.3.1 Translation Along ML Axis

The load curve for the lateral part of the translational direction in the ML DOF, Figure 3.1a, is a force-displacement curve created by extracting force and displacement from Figures A1.1 and A1.2 in Koh et al. (2004).

The medial part was modelled as a straight line from -40 N to the origin. Since the displacement was needed to create the line, and not given directly in the literature, it was calculated by dividing the force by the stiffness from Figure 3F in Goodine et al. (2022). The reasons that we chose to use the stiffness for the intact AC joint is based on the assumption that the contribution of the conoid and trapezoid ligaments is assumed to be negligible, as well as that they are not yet implemented in the current VIVA+ model for compression. By using the stiffness for the intact AC joint, these contributions will be accounted for with the new AC joint.

3.1.3.2 Translation Along AP Axis

The load curve for the translation in AP direction, shown in Figure 3.1c, was determined from two curves in Figure 2 in Flores et al. (2023). The first curve "AP translation intact" is a force-displacement curve where they tested all the ligaments such as AC, conoid, and trapezoid ligaments. In the second curve "AP translation conoid + trapezoid", the AC ligament was cut, meaning that only the conoid and trapezoid ligaments were tested. By subtracting the second load curve from the first, a force-displacement curve was extracted for the AC ligament only, this is what was used for the AP translation load curve.

To extract the values for the load curve, the mentioned curves from Flores et al. (2023) were first digitised with the help of Automeris (https://automeris.io/). Adjustments were made so that both curves passed through the origin before they were subtracted. The difference of the two curves were plotted and the y-axis was scaled by a factor 0.001 to get the correct unit in LS-DYNA (kN and mm).

3.1.3.3 Translation Along SI Axis

The superior part of the load curve for translation along the SI axis is shown in Figure 3.1e. It is a bilinear elastoplastic curve generated by using the mean values of yield load and deformation, and ultimate load and deformation from the specimens with the CC ligament cut, from Dawson et al. (2009). These values are presented in Table 3.1. After creating this bilinear curve, a ramp-up was implemented to avoid numerical instability due to discontinuity at the origin and the yield point, see Appendix Table A.1.

Table 3.1: Mechanical properties for specimens with the CC ligament cut and the AC ligament intact (Dawson et al., 2009).

Parameter	Load (kN)	Deformation (mm)
Yield	0.213	6.3
Ultimate	0.346	13.4

The inferior stiffness for the SI translation is a straight line determined from Goodine et al. (2022). For this load curve the stiffness was determined by subtracting the stiffness value from the test with the AC ligament cut from the stiffness value with all ligaments intact. This stiffness was defined for compressive loads up to -0.07 kN.

3.1.3.4 Rotation Around ML Axis

No published data in literature was found for the rotation around the ML axis. This was approximated to 1 Nm/deg which is approximately 10 times stiffer than the external rotation, as shown in Figure 3.1b. The stiffness was assumed because of the AP part of the AC ligament that prevents it in these movements, which the rotation around the ML axis includes.

3.1.3.5 Rotation Around AP Axis

For the load curve for the rotation around the AP axis there were no values available in the literature. The value was approximated to be zero, see Figure 3.1d. This was assumed due to the fact that there are no major ligament structures that prevents movement around the AP axis, therefore it can rotate freely.

3.1.3.6 Rotation Around SI Axis

The values of the load curve for rotation in the SI direction were derived from Flores et al. (2023) for the internal direction, while the superior rotation was extracted from Morikawa et al. (2020). The resulting load deflection curve is shown in Figure 3.1f. The external rotation was based on 0.096 Nm/deg.

3.2 Verification of the Acromioclavicular Joint

To confirm that the implementation of the AC joint was aligned with the physical reality of the joint, four different DOFs were verified against existing experiments (Flores et al., 2023; Koh et al., 2004). The DOFs that were verified were ML, SI, AP translation, and SI rotation.

3.2.1 Lateral Translation

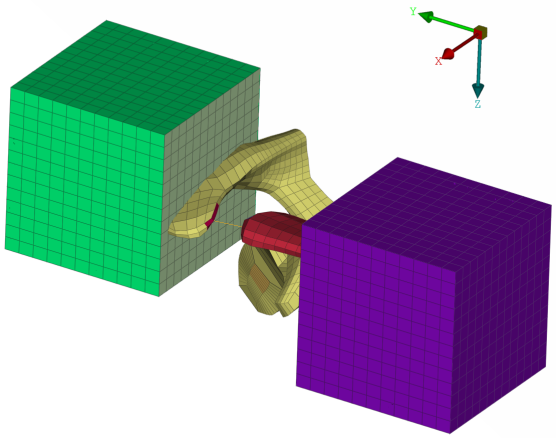

Figure 3.2: Sub-model used for lateral translation test, replicating Koh et al. (2004).

The sub-model used for the tensile testing of the ligament in the AC joint consisted of the scapula, the clavicle, and two potting cups filled with resin. The trapezoid and conoid ligaments where removed from the submodel. See Figure 3.2.

In Koh et al. (2004), the SC, AC, and CC joints were tested using a high-speed hydraulic machine at the three different strain rates, a quasi-static rate and two high-rates, high-rate 1 and 2. The ligaments were clamped on both sides, with a load cell on one side to record tensile force. The ligaments were oriented so that the force from the machine was applied along the longitudinal axis of the ligament.

To verify the implementation of the ligament, a simulation was performed to replicate the high-rate 1 (5.87 m/s) tensile loading from Koh et al. (2004). The two potting cups filled with resin were attached to the scapula and the clavicle, respectively. The potting cup attached to the scapula was fully constrained, meaning it could not move. The potting cup attached to the clavicle was fixed for rotation in all DOFs and for translation in SI and AP. It was given a velocity with a ramp-up, see Appendix Table A.1. The ramp-up was used to both avoid numerical instability, and to be able to adjust the acceleration. The y-axis was then scaled to 5.87 to match the loading rate of (Koh et al., 2004). To reduce oscillatory response, the x-axis was also scaled to 4. Because of this scaling the targeted velocity was reached within the simulation but at a slower rate. To further reduce oscillation, the mass of the potting cup and the resin were reduced. The displacement was measured for the distal rigid part of the clavicle before and after the tensile test, and the force was measured from the potting cup of the clavicle (Koh et al., 2004).

3.2.2 Translation Along SI & AP Axis and Rotation Around SI Axis

In Flores et al. (2023), force-displacement in inferior translation, AP translation, and inferior rotation was measured on six shoulders from PMHS. Only the AC and CC ligaments were preserved in the shoulder; the rest of the tissue was dissected. To perform the tests, the scapula was potted in bone cement on a testing machine which has a six DOFs test platform that can control force and displacement. The clavicle was fixed on the arm of the testing machine. A coordinate system was implemented in the test and aligned with the clavicle: the x-axis was aligned with the bone, the y-axis pointed backwards (posterior direction), and the z-axis pointed downwards (inferior direction). For the mechanical tests, the testing machine moved the joint very slowly (0.1 Hz) while measuring the movement. For the inferior translation, the scapula was pushed downward with a force of 20-70 N. For the AP translation, the scapula was pushed forward and then backward with a force of 40 N. For the internal rotation, the scapula was rotated by about 15 degrees.

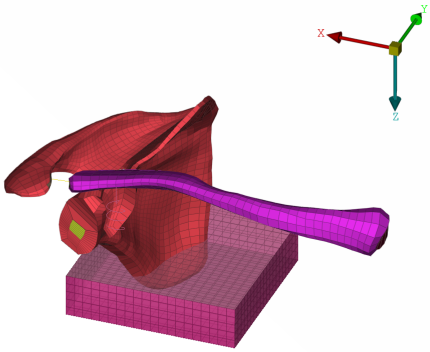

Figure 3.3: Test setup replicated from Flores et al. (2023).

The model was created to replicate the Flores et al. (2023) setup as close as possible. The model contained one potting cup filled with resin, to which the scapula is attached. The AC ligament attached the clavicle to the scapula, see Figure 3.3. Four simulations (AP translations, inferior translation and inferior rotation) were made to emulate the different tests.

The first simulation was the inferior translation. The scapula potting cup was constrained in ML translation and ML, AP, and SI rotation. A velocity was applied to the potting cup in the inferior direction. The velocity curve implemented was the same ramp-up, with the x-axis scaled by 15 and y-axis scaled by 0.25. There was no velocity given in Flores

et al. (2023), therefore this is an estimation to reach the targeted force and to balance the inertial effects. The rigid part of the clavicle was fully constrained in all directions. The displacement was measured from the rigid part of the scapula where the ligament connects, before and after the translation. The force was measured continuously from the potting cup that was attached to the scapula.

The second simulation was the AP translation. The potting cup was constrained in ML and SI translation, and ML, AP, and SI rotation. The same ramp-up (Appendix, Table A.1) was implemented as a velocity curve and applied to the potting cup in the anterior translation. The x-axis was scaled by 25 while the y-axis was scaled by 0.5. As previously stated there was no velocity given in Flores et al. (2023), therefore this is an estimation to reach the targeted force and to balance the inertial effects. The rigid part of the clavicle was fully constrained, and the force and displacements were measured from the same parts as for the inferior translation. The third simulation had the same setup but the velocity applied in the posterior direction instead.

In the fourth simulation the scapula was fully constrained. The velocity was applied to the clavicle as an inferior rotation. The clavicle was constrained fully in translation and in ML and AP rotation. The velocity curve (Appendix, Table A.1) was scaled by 20 on the x-axis and 0.025 in the y-axis. This is an estimation to reach the targeted force and to balance the inertial effects. The rotation was measured between the distal end of the clavicle and a point on the clavicle near the conoid ligament. The torsional moment was measured between the same point and the rigid part of the clavicle. Both the conoid and the trapezoid ligaments attaching the clavicle and scapula were removed.

3.3 Sternoclavicular Joint Implementation

In this section, the implementation of the SC joint is described. Experiments from Negri et al. (2014) and Spencer and Kuhn (2004) were simulated for verification.

3.3.1 Placing of Ligament

The old robotic joint was removed. The beam was then placed between the superior sternum, manubrium, and the medial part of the clavicle on their respective rigid parts.

3.3.2 Coordinate System

A local coordinate system was established to align with the global coordinate system of the VIVA+ model, which corresponds to the anatomical ML, AP, and SI directions. The origin of the coordinate system was positioned at the centre of the superior region of the sternum, serving as the centre of rotation for the SC joint.

3.3.3 Load Curves

The load curves were obtained from Goodine et al. (2022), Koh et al. (2004), Negri et al. (2014), and Spencer and Kuhn (2004), and are shown in Figure 3.4. In the following sections it is further described how these were derived.

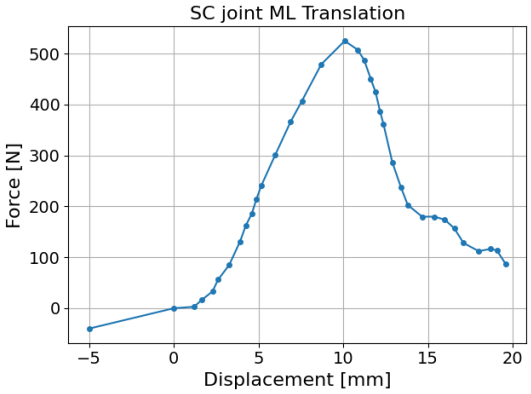

(a) ML translation

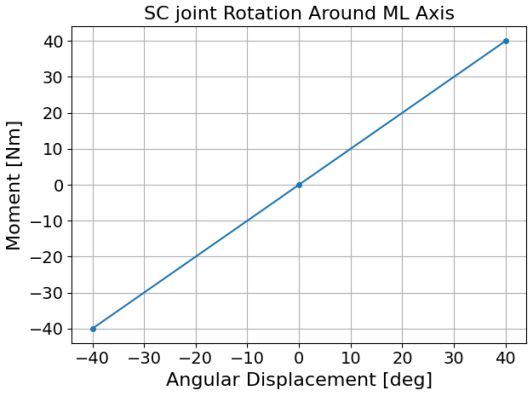

(b) ML Rotation

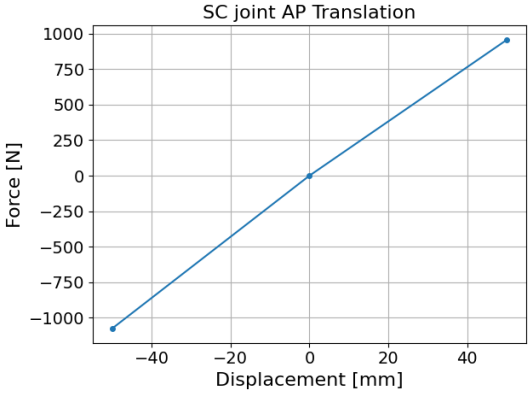

(c) AP Translation

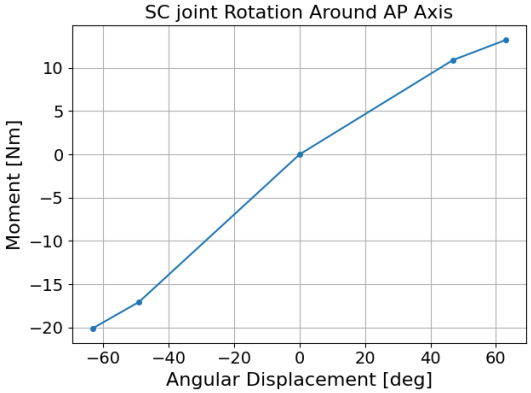

(d) AP Rotation

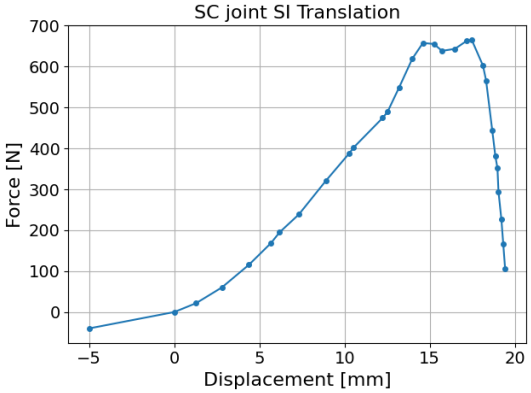

(e) SI Translation

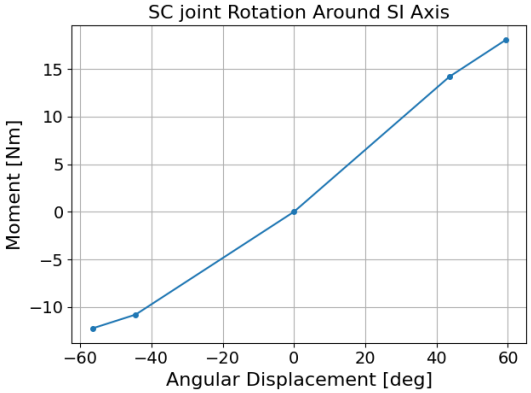

(f) SI Rotation

Figure 3.4: Translation and rotational load curves for SC joint.

3.3.3.1 Translation Along ML Axis

The load curve for lateral translation, showed in Figure 3.4a, was generated from the force-displacement curves in Figures A1.5 and A1.6 from Koh et al. (2004). Figure A1.5 describes the force time history of a right SC joint at high-rate 1 (5.87 m/s), and Figure A1.6 describes the displacement time history of an SC joint at high-rate 1. To obtain the force-displacement curve, the two figures were cross-plotted.

For the medial part of the ML translation, there was no literature found providing information about the mechanical properties. An assumption was made that the load curve for AC medial translation would have similar properties as SC medial translation, and since there were more data published on the AC joint it was used for this joint as well.

3.3.3.2 Translation Along AP Axis

To create the load curve for the AP translation, a mean stiffness of the SC ligament was calculated from multiple test subjects in the study by Spencer and Kuhn (2004). The study first tested the intact ligament for AP subfailure translation, only average stiffness values were available and used. The mean was calculated from 18 subjects and was 19.1 N/mm for anterior translation and 21.5 N/mm for posterior translation. To obtain points for the load curve, a 50 mm displacement was chosen for both posterior and anterior translation. The resulting load curve for this loading direction is presented in Figure 3.4c.

3.3.3.3 Translation Along SI Axis

For translation along the SI axis there were no literature found. For the inferior translation, it was assumed that the mechanical properties would be similar to the ones for medial translation in the AC joint, and that same load curve was implemented.

The superior translation in the SC ligament was considered similar to the lateral translation in the AC ligament. Since there were no data available for the SC joint, the data for the lateral translation in the AC joint was used. The load curve is presented in Figure 3.4e

3.3.3.4 Rotation Around ML Axis

No literature were found describing rotation around the ML axis of the SC joint. The ligament was presumed to be stiff in rotation around this axis and therefore approximated to 1 Nm/degree in the load curve, as shown in Figure 3.4b. This was assumed because the CC ligament provides stability between the clavicle and the anterior first rib, which directly affects the ML rotation to be stiff.

3.3.3.5 Rotation Around AP Axis

For the rotation around the AP axis, values were obtained from Negri et al. (2014), that examined primary and secondary failures of the SC joint in depression (movement of the shoulders, superior to inferior) and elevation (movement of the shoulders, inferior to superior). The values were used to create bilinear curves. For the rotation from an inferior to a superior position around the AP axis, the elevation values from Negri et al. (2014) were used. The ultimate point, the torsional moment at the maximum resistance limit (TMRL) was 13.21 Nm, and the angular displacement at the proportional limit (ADRL) was 62.96 degrees. For the yield point, the torsional moment at the proportional limit (TMPL) was 10.90 Nm, and the angular displacement at the proportional limit (ADPL) was 46.90 degrees for elevation.

For the rotation from a superior to an inferior position around the AP axis, the depression values from Negri et al. (2014) were used, with TMRL at 20.10 Nm and ADRL at 63.28 degrees. For the yield point, TMPL was 17.04 Nm, and ADPL was 49.08 degrees (Negri et al., 2014). To model this as a single load curve for the entire rotation around the AP axis, Figure 3.4d, the values for depression were multiplied by -1.

3.3.3.6 Rotation Around SI Axis

For the rotation around the SI axis, data from Negri et al. (2014) was used. The retraction (movement of the shoulders, anterior to posterior) and protraction (movement of the shoulders, posterior to anterior) were both modelled as bilinear curves. For the rotation from a posterior to an anterior position around the SI axis, values for protraction was used. TMRL is 18.04 Nm, ADRL is 59.35 degrees, TMPL was 14.19 Nm, and ADPL was 43.61 degrees.

For the rotation from an anterior to a posterior position around the SI axis, values for retraction in Negri et al. (2014) was used. TMRL was 12.25 Nm, ADRL was 56.54 degrees, TMPL was 10.80 Nm, and ADPL was 44.42 degrees. The values for inferior rotation were multiplied by -1 to create a load curve for the whole rotation around the SI axis, Figure 3.4f.

3.4 Verification of SC Joint Implementation

To confirm that the implementation of the SC joint was aligned with the physical reality of the joint, three different DOFs were verified against already existing experiments (Negri et al., 2014; Spencer & Kuhn, 2004). The DOFs that were verified were rotation around the SI and AP axis, and AP translation.

3.4.1 Rotation Around SI and AP axis

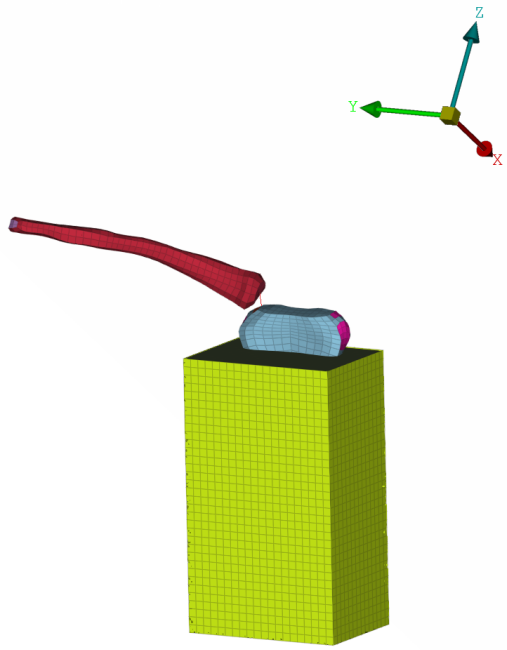

Figure 3.5: LS-DYNA setup with the sternum and clavicle for the SI and AP rotation simulation.

The test setup from Negri et al. (2014) was replicated (see Figure 3.5) to verify the rotation around the SI axis and rotation around AP axis. They tested 12 ligaments each in four movements: elevation, depression, protraction, and retraction. The ligaments were harvested from PMHS. The specimens consisted of the sternum, the first rib, parts of the coastal cartilage and the clavicle, with muscles removed. The sternum was placed in a plastic potting covered in polymethylmethacrylate (PMMA) and attached to a rectangular claw. The claw also had a cylindrical tube where the clavicle was inserted. To create the torsional moment needed for testing rotation, a cable was attached to a pulley in one end and a load cell in the other. The movement of the load cell caused rotational movement in the pulley which moved the acromial end of the clavicle (Negri et al., 2014). From each test the following values were reported: torsional moment and angular displacement at the maximal resistance limit, and torsional moment and angular displacement at the proportional limit (Negri et al., 2014).

To replicate this test, the sternum together with the left clavicle was modelled in LS-DYNA, see Figure 3.5. The sternum was placed in a rectangular potting cup. It was placed so that the SC joint and the manubrium were outside of the pot. There were no values of

mechanical properties reported in Negri et al. (2014) for PMMA, and the mechanical properties for this had be derived from similar material. To be able to apply the load at the distal end of the clavicle, a rigid part was created. The load was applied as a velocity, with a ramp-up (Appendix, Table A.1). For elevation and depression, the velocity was applied around the SI axis whereas for protraction and retraction it was applied around the AP axis. The rigid part at the proximal end of the clavicle was constrained in the three translational directions and free in all rotational directions.

The angular displacement was measured at the proximal end of the clavicle from the coordinate system located at the mid of the manubrium, whereas the torsional moment was measured between the medial and distal part of the clavicle. These values were plotted into a graph and compared to the two points reported in Negri et al. (2014) for each test.

3.4.2 Translation Along AP Axis

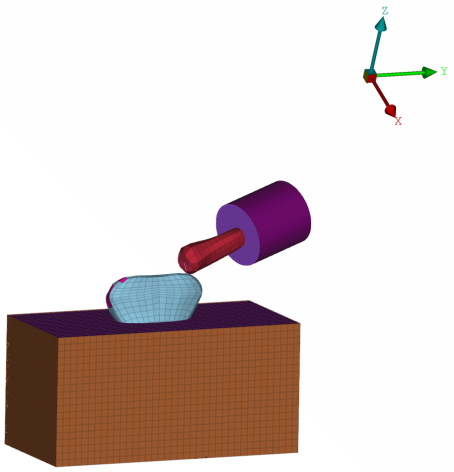

Figure 3.6: LS-DYNA setup with the sternum and clavicle for translation along AP axis simulation.

The test set up from Spencer and Kuhn (2004) was replicated, see Figure 3.6, to verify the translation along the AP axis. In the study, 36 SC joints were tested using a custom setup, in which the specimens were tested under displacement control. For the setup, the sternum was secured in a rectangular aluminium pot filled with PMMA. The clavicle was potted separately using PMMA in a polyvinyl chloride cylinder, reaching the height of the CC ligament. After potting, the specimens were placed in a custom testing fixture. The sternum potting was secured to the base of the testing machine. The potted clavicle was attached to the actuator. The actuator was programmed to apply displacement-controlled

movement and to record the force exerted on the specimens. The displacement was applied at a constant rate of 0.25 mm/s. The testing fixture included a ball-bearing plate that allowed the sternum for slight ML translation. A load cell was applied to the actuator to measure the force. The displacement was measured from the actuator.

To replicate the setup used by Spencer and Kuhn (2004), the sternum was placed in a rectangular potting cup with dimensions identical to the experiment. The potting cup was modelled as aluminium. The properties of the resin filling the potting cup were not specified in the original study, so they had to be estimated. Similarly, the clavicle was positioned in a cylinder with assumed material properties, and the resin filling this cylinder also required estimation. A summary of the material properties used in the model is provided in Appendix, Table A.2. The model was aligned with the anatomical position, the global anatomical coordinate system in LS-DYNA. The aluminium potting cup containing the sternum was completely fixed in all DOFs. A load was applied to the cylindrical potting in which the clavicle was embedded. The load was applied as a velocity using a ramp-up curve that was scaled with 20 on the x-axis and 0.25 on the y-axis. The displacement was measured from where the SC joint attaches to the clavicle. The force was measured from the aluminium potting cup.

3.5 Biomechanical Response Corridors

This section describes the full pipeline used to construct the biomechanical response corridors. The workflow consisted of four main steps: data processing, dimension reduction using PCA, Bayesian regression of the PC scores and final construction of the corridors.

3.5.1 Data Processing

The data processing phase began with digitising different figures from Compigne et al. (2004). This was done to convert published force-time and deflection-time curves into numerical data that could be used in the analysis. Each curve was imported into Automeris (https://automeris.io/), where the curves were digitised and saved as separate CSV files.

The digitised curves were interpolated to a common time grid. The interpolation was performed separately for each measurement type, so that all force curves had the same force time grid and all deflection curves had the same deflection time grid. This is needed for the following PCA where all the curves have to be vectors with the same number of time steps.

The interpolated curves were combined into one dataframe for each measurement, where each row represented one subject at a specific angle and velocity. Information about the

subjects, such as sex, weight, height, etc. was also added to the dataframe.

3.5.2 Principal Component Analysis

The obtained dataframe was divided into two separate dataframes. One contained the numerical data, and the other contained the information about test conditions and subject features. This separation made it possible to analyse the curves independently while still keeping the condition and subject information available for interpretation.

The numerical data was used as input for the PCA, which was used to describe the curves using a smaller number of PC scores. These scores were added to a new dataframe, together with the information about conditions and subject features.

The PCA results, including explained variance ratio, were analysed to determine how many PCs were needed to describe as much of the variation in the data as possible. The root mean square error (RMSE) between the reconstructed and original curves were used as an additional evaluation of how many PCs to use.

After the evaluation, the selected PCs were interpreted by studying reconstructed curves to understand what type of behaviour each component captured in the response. The PC scores were also compared with subject features to explore possible relationships between the response and subject variables.

3.5.3 Bayesian Regression

Bayesian regression was used to model the PC scores as functions of velocity, angle and subject features. Each PC score was treated as individual response variables, which allowed to analyse the variations in the curves separately.

Since there were several response curves for each subject, multilevel regression was used with subject as the grouping variable. This allows the model to account for subject-specific variation in the general response level. Several candidate models were fitted for each PC score to identify which experimental conditions and subject features contributed to the variation in the response curves. All models included a subject-specific intercept to account for repeated observations from the same subject.

The same set of candidate models was tested separately for each selected PC, and the models were compared using approximated LOO. The tested model structures are shown in Table 3.2, with the subject-specific intercepts denoted as (1|subject) in the formulas.

Table 3.2: Candidate regression models used for the PC scores.

Model	Formula
Velocity	$PC_i \sim \text{velocity} + (1\|\text{subject})$
Velocity + weight	$PC_i \sim \text{velocity} + \text{weight} + (1\|\text{subject})$
Velocity + flesh thickness	$PC_i \sim \text{velocity} + \text{flesh} + (1\|\text{subject})$
Velocity + sex	$PC_i \sim \text{velocity} + \text{sex} + (1\|\text{subject})$
Velocity + sex + flesh thickness	$PC_i \sim \text{velocity} + \text{sex} + \text{flesh} + (1\|\text{subject})$
Velocity + angle	$PC_i \sim \text{velocity} + \text{angle} + (1\|\text{subject})$
Angle	$PC_i \sim \text{angle} + (1\|\text{subject})$
Angle + sex	$PC_i \sim \text{angle} + \text{sex} + (1\|\text{subject})$

The regression models were implemented in Python using Bambi (Capretto et al., 2022), a Bayesian model-building interface, with the PyMC (Abril-Pla et al., 2023) probabilistic programming framework. Posterior sampling was performed using NUTS, with several chains and a fixed number of tuning and draws. The tuning is used as warm up, where NUTS try to adapt to the shape of the posterior, and draws are the actual samples. To reduce the risk of divergence, a higher target acceptance rate was used. The acceptance rate decides how cautious NUTS should be during the warm up.

3.5.4 Construction of Corridors

The corridors were created so that different scenarios could be evaluated with the same procedure. The scenario was different fixed combinations of angle, velocity and sex. The selected model for each PC were used to produce posterior samples for the specific scenarios.

In the corridor construction, two method choices were evaluated. The first one was what type of distribution to use for the PC scores. Posterior predictive samples were compared with the posterior samples of the expected response. The second one was to decide if the corridor boundaries should be calculated in PC-space or curve-space.

The PC-space method computes the Highest Density Interval (HDI) of the posterior PC samples. An HDI is the narrowest interval that includes a specified amount of the posterior distribution. This means that all the points inside the HDI have a higher probability density than the points outside of it (Martin et al., 2024). The most probable PC scores were reconstructed to response curves using inverse PCA transformation, and the corridor was obtained by taking the envelope of all the reconstructed curves. The envelope is an upper and lower bound outlining all the extreme values. The curve-space method reconstructs all the posterior PC samples into response curves and computes the corridor bounds as the HDI of the curves for each time step. For the final corridors, the lower boundary was constrained to zero since the force is treated as a contact force.

3.6 Implementation in VIVA+ Model

After verifying the AC and the SC joints by comparing the simulations to the experimental data, they were implemented in the full VIVA+ model. First, the old robotic joints were removed from the model. Then the new AC and SC joints were implemented on the same nodes as in the submodels, and the load curves were implemented with a small adjustment. The unloading part from the load curves for SI and ML translation for SC joint, and ML translation for AC joint were removed, see Figure 3.7, 3.8 and 3.9.

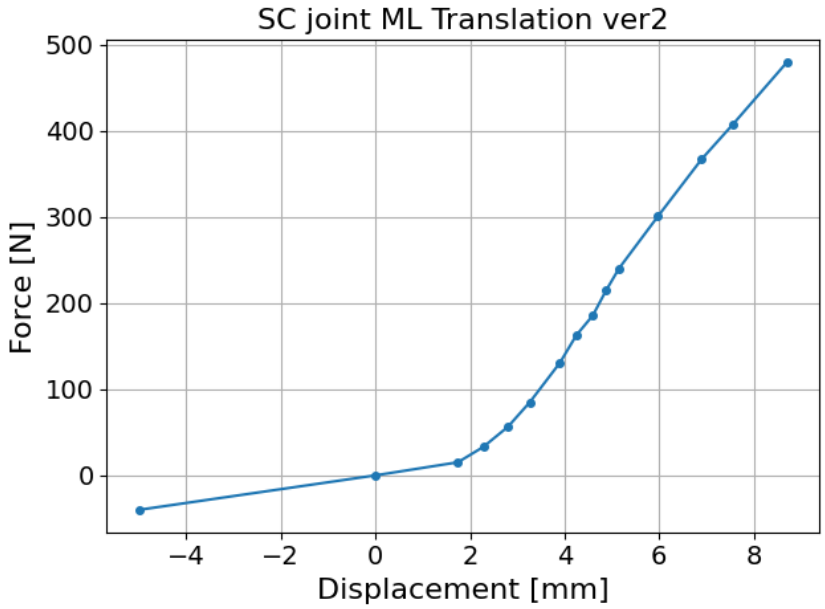

Figure 3.7: The new version of the load curve for ML translation of the SC joint. It is the same curve as before, but without the unloading part.

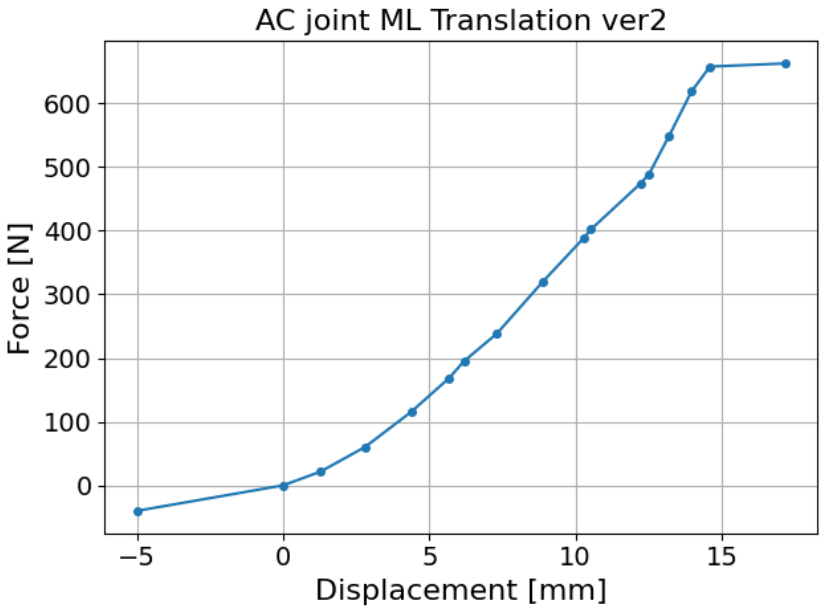

Figure 3.8: The new version of the load curve for ML translation of the AC joint.It is the same curve as before, but without the unloading part.

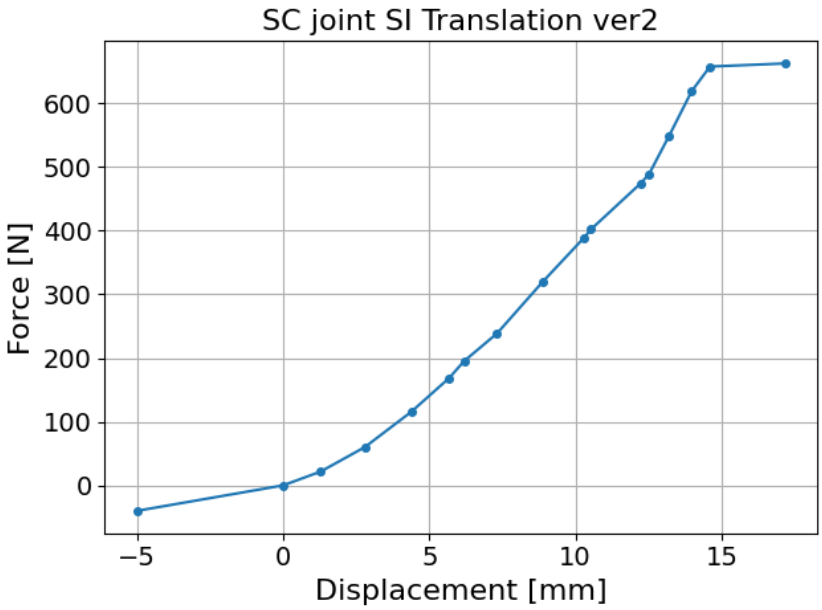

Figure 3.9: The new version of the load curve for SI Translation of the SC joint. It is the same curve as before, but without the unloading part.

3.7 Validation of Biofidelity in VIVA+ Model

In Compigne et al. (2004), an impact test was performed on PMHS to examine shoulder response in side impacts. The test included seven PMHS seated and exposed to a lateral impact at different speeds and angles. A low-speed test was conducted at 1.5 m/s with

angles of -15, 0, and 15 degrees. Then a high-speed test was performed at speeds between 3 m/s and 6 m/s and at only 0 degrees. To measure the shoulder's reaction to the impact, a tri-axial accelerometer was placed on different parts of the shoulder. It could track how these parts moved relative to each other in different directions. In the same positions as the tri-axial accelerometer, photographic markers were placed and could be captured by a 3D camera.

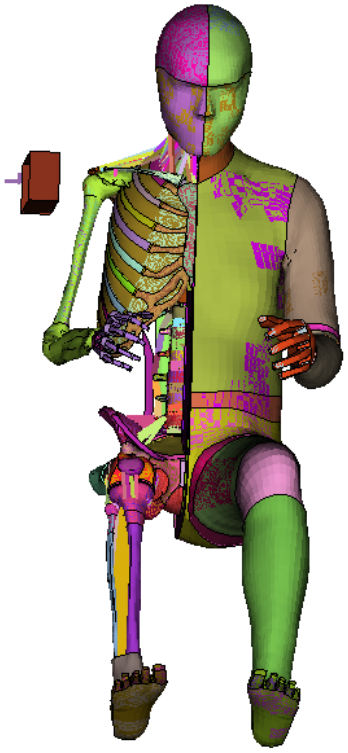

Figure 3.10: VIVA+ model in the Compigne et al. (2004) impact test. Some soft tissues on the right side were removed for visual purposes only.

To replicate Compigne et al. (2004), see Figure 3.10, several simulations were run, comprising two models: a 50-th percentile female and a 50-th percentile male, at three different velocities: 1.5 m/s, 3 m/s, and 6 m/s at 0 degree angle. The load curves and local coordinate systems from two submodels of the AC and SC joints were integrated into the new models. The primary measurement in the study was the acromion-to-acromion deflection, defined as the resultant displacement between the left and right acromion. To replicate this, nodes located on the acromions were tracked. The distance between the two nodes was calculated by measuring their coordinates in the x-, y-, and z-axes and applying the Pythagorean theorem. Initially, the distance was recorded, and as the simulation progressed, the new distance was recalculated every millisecond. The deflection value was then calculated by subtracting the initial value from the new values. The response corridors were plotted together with the simulated data.

4

Results

In this chapter the different results for verifying the individual joints in various directions are presented first. Then, the results of the corridor construction, including PC and regression analysis, are presented. Lastly, the results from the full body impact test with both joints implemented are presented together with the created corridor.

4.1 Verification of Acromioclavicular Joint

In the following section, the results from verification of the isolated AC-joint are presented. The tests that were replicated were Flores et al. (2023) and Koh et al. (2004).

4.1.1 Lateral Translation

Figure 4.1 shows the result from the lateral translation verification based on Koh et al. (2004). The figure shows the simulated data compared to the experimental data extracted from Koh et al. (2004). The simulated result is in good agreement with the experimental curve.

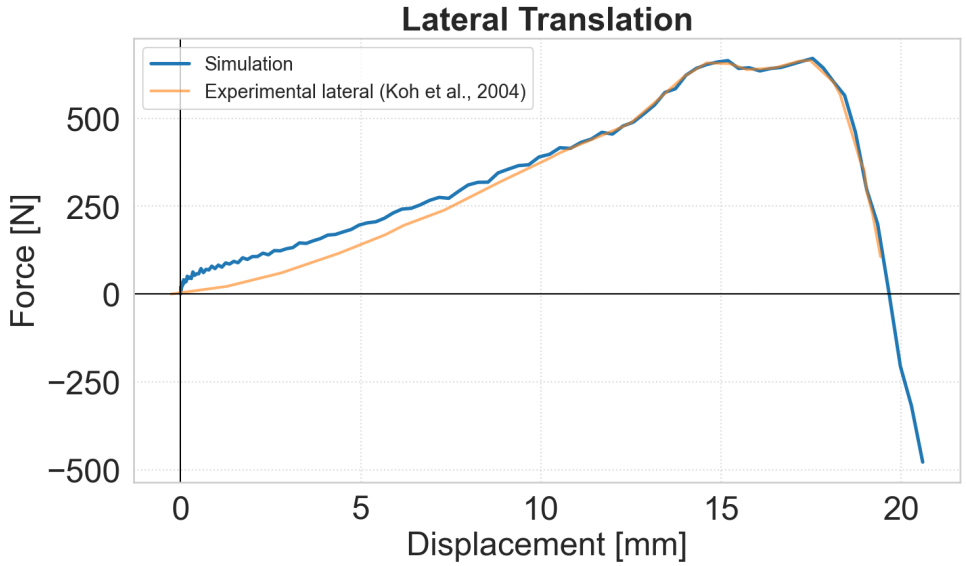

Figure 4.1: Comparison between simulated and experimental results in lateral translation for AC ligament. The experimental values were extracted from Figure A1.1 and A1.2 in Koh et al. (2004).

4.1.2 Inferior Translation

Figure 4.2 shows the result from the inferior translation verification, based on Flores et al. (2023). This figure compares the simulated data to the calculated stiffness of the experimental curve. The stiffness for both the simulation and experimental data is calculated by using Equation (2.2) between 20-70 N. The data used to calculate and the stiffnesses is presented in Table 4.1. The difference between the calculated stiffness for the simulation and the experiment is minimal.

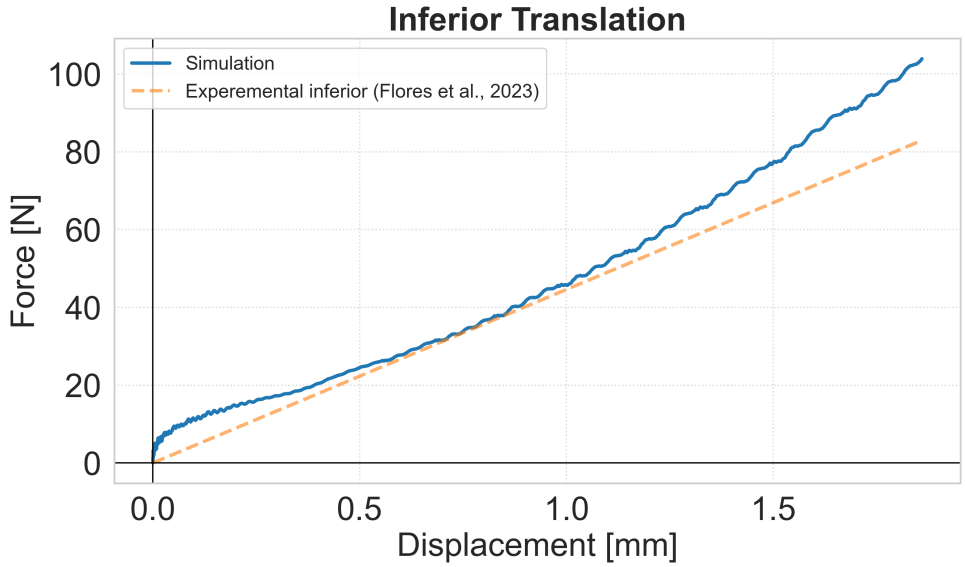

Figure 4.2: Comparison between simulated and experimental results in inferior translation for the AC ligament. The experimental value was extracted from Figure 2 in Flores et al. (2023).

Table 4.1: Calculated inferior translational stiffness values based on force–displacement response between 20-70 N . Comparing experimental data from Flores et al. (2023) to simulated result.

Dataset	Dir	F_0 [N]	d_0 [mm]	F_1 [N]	d_1 [mm]	K [N/mm]
Experimental	Inferior	20.00	3.00	69.03	4.10	44.6
Simulation	Inferior	20.00	0.39	70.01	1.39	50.01

4.1.3 Translation Along AP Axis

Figure 4.3 shows the result for AP translation verification based on Flores et al. (2023). It compares the simulated data to experimental data extracted from Flores et al. (2023). The siffness for the curves are calculated by using Equation (2.2) between 20-40 N. The data used to calculate and the stiffnesses is presented in Table 4.2. The simulated and experimental stiffness are in close agreement and only differ minimally

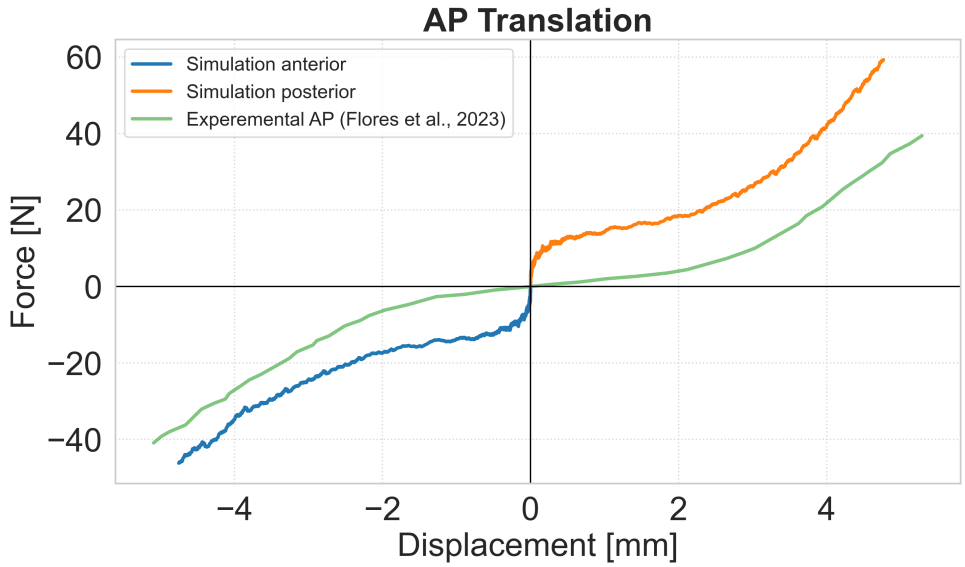

Figure 4.3: Comparison between simulated and experimental results in AP translation for the AC ligament. The experimental value was extracted from Figure 2 in Flores et al. (2023).

Table 4.2: Calculated AP translational stiffness values based on the force–displacement response between 20 and 40 N, comparing experimental data from Flores et al. (2023) with simulated results.

Dataset	Dir	F_0 [N]	d_0 [mm]	F_1 [N]	d_1 [mm]	K [N/mm]
Experimental	Posterior	20.88	3.94	39.41	5.29	13.73
Experimental	Anterior	-20.59	-3.42	-40.88	-5.09	12.15
Simulation	Posterior	20.00	2.36	40.02	3.90	13.00
Simulation	Anterior	-20.00	-2.46	-40.00	-4.24	11.24

4.1.4 Inferior Rotation

Figure 4.4 illustrates the inferior rotation verification based on Flores et al. (2023). It shows a comparison between simulated data and experimental data from Flores et al. (2023). The simulated response was obtained without including the conoid ligament. There is two experimental curves. “Experimental - intact (Flores et al., 2023)” includes all ligaments. The curve denoted as “Experimental - altered (Flores et al., 2023)” was created by computing the difference between the intact internal rotation response and the internal rotation response with the conoid and trapezoid ligaments in Flores et al. (2023).The stiffnesses is presented in Table 4.3. Both simulation and experimental curves showed similar response although the magnitude of moment is approximately 2 Nm higher in the simulation response.

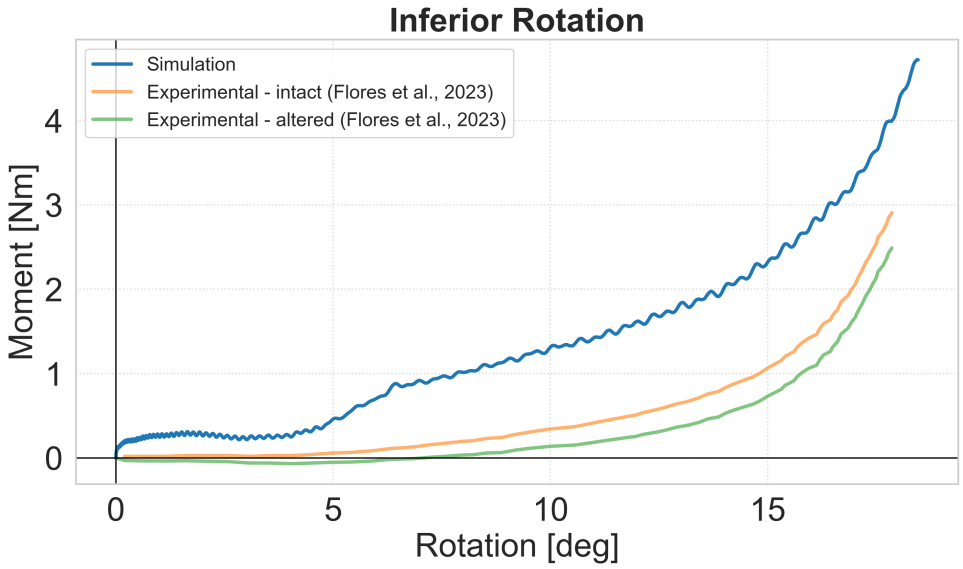

Figure 4.4: Comparison between simulated and experimental results in inferior rotation for AC ligament. The curve "Experimental - intact (Flores et al., 2023)" was extracted from Figure 3 in Flores et al. (2023). The curve "Experimental - altered (Flores et al., 2023)" was calculated by computing the difference between the response with the intact shoulder and the response with the AC ligament removed Figure 3 in Flores et al. (2023).

Table 4.3: Calculated rotational stiffness values based on the moment–rotation response between 0° and 15°. Comparing experimental data from Flores et al. (2023) with simulated results.

Dataset	R_0 [deg]	M_0 [Nm]	R_{15} [deg]	M_{15} [Nm]	K [Nm/deg]
Simulation	0.00	0.00	15.00	2.32	0.155
Experimental – intact	0.00	0.02	15.00	1.06	0.070
Experimental – altered	0.00	0.00	15.00	0.73	0.049

4.2 Verification of Sternoclavicular Joint

In the following section the results for the isolated SC joint verification are presented.

4.2.1 Rotation Around SI Axis

Figure 4.5 presents the result of the SI rotation validation based on Negri et al. (2014). The figure shows a comparison between experimental values from Negri et al. (2014) and simulated response for retraction and protraction. The stiffness is calculated and presented in Table 4.4. The results are in good agreement. Only a minimal difference is observed between the simulated and experimental stiffness values.

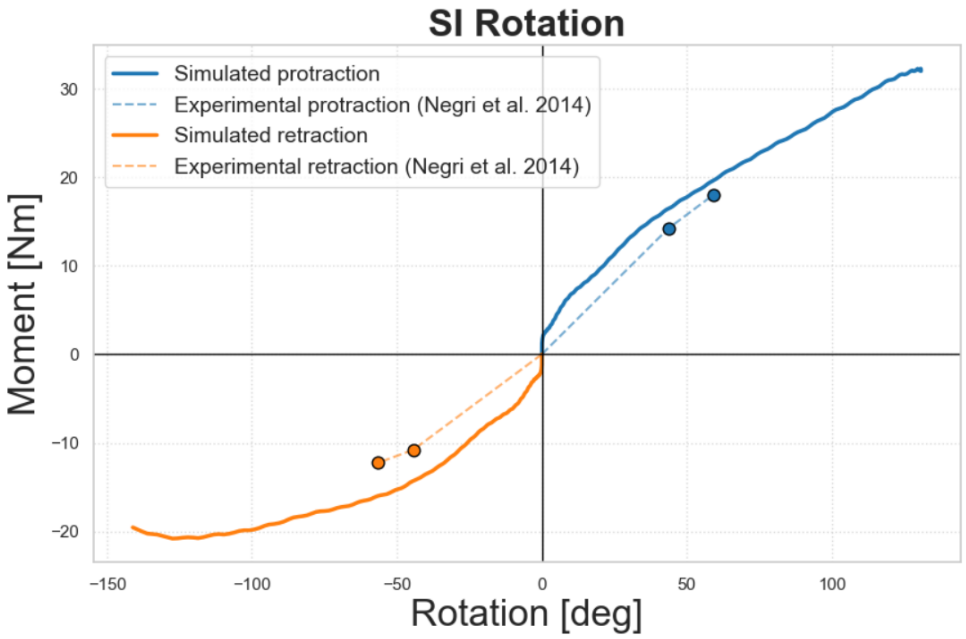

Figure 4.5: Comparison between simulated and experimental results in SI rotation for the SC ligament. The experimental values was extracted from Table 2 in Negri et al. (2014).

Table 4.4: Calculated rotational stiffness for simulated and experimental data in SI rotation verification for protraction and retraction. Evaluated separately for yield and ultimate regions.

Dataset	Dir	R_0 [deg]	M_0 [Nm]	R_1 [deg]	M_1 [Nm]	K [Nm/deg]
Simulation yield	Protraction	0.855	2.62	36.9	15.2	0.349
Experimental yield	Protraction	0.00	0.00	43.61	14.19	0.325
Simulation ultimate	Protraction	36.9	15.2	60.6	20.2	0.211
Experimental ultimate	Protraction	43.61	14.19	59.35	18.04	0.245
Simulation yield	Retraction	-0.389	-1.98	-49.02	-14.95	0.267
Experimental yield	Retraction	0.00	0.00	44.42	10.80	0.243
Simulation ultimate	Retraction	-49.02	-14.95	-120	-20.4	0.076
Experimental ultimate	Retraction	44.42	10.80	56.54	12.25	0.119

4.2.2 Rotation Around AP Axis

Figure 4.6 displays the result of AP rotation verification based on Negri et al. (2014). The figure compares the simulated results to experimental data extracted from Negri et al. (2014) in elevation and depression. The stiffness is calculated and presented in Table 4.5. Good agreement is observed between the simulated and experimental stiffness values, with only a small difference between the datasets.

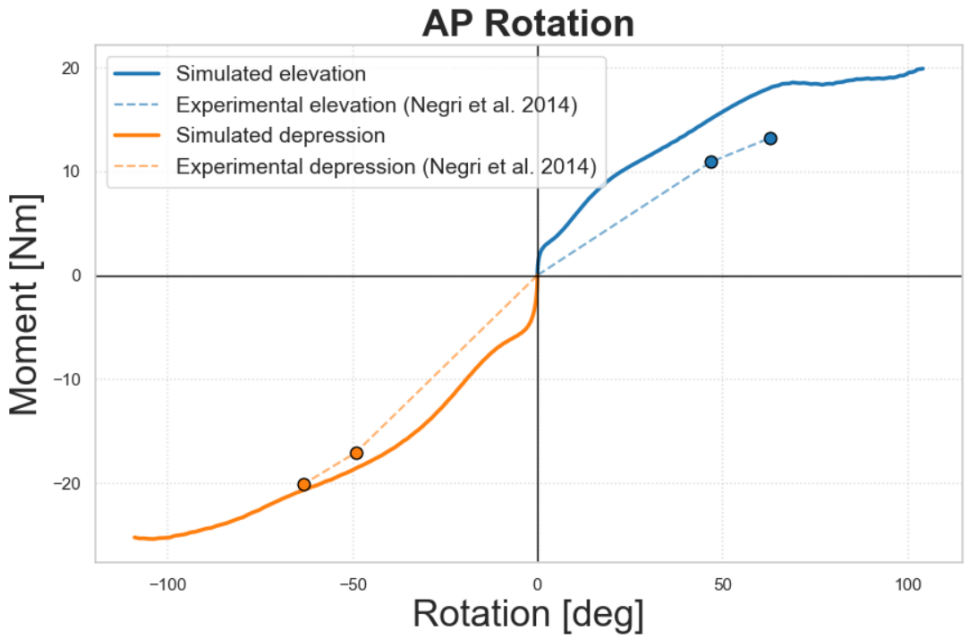

Figure 4.6: Comparison between simulated and experimental results in AP rotation for the SC ligament. The experimental values was extracted from Table 2 in Negri et al. (2014).

Table 4.5: Calculated rotational stiffness for simulated and experimental data in AP rotation verification for protraction and retraction. Evaluated separately for yield and ultimate regions.

Dataset	Dir	R_0 [deg]	M_0 [Nm]	R_1 [deg]	M_1 [Nm]	K [Nm/deg]
Simulation yield	Elevation	1.41	2.79	68.8	18.4	0.232
Experimental yield	Elevation	0.00	0.00	46.90	10.90	0.232
Simulation ultimate	Elevation	68.8	18.4	102	19.7	0.039
Experimental ultimate	Elevation	46.90	10.90	62.96	13.21	0.144
Simulation yield	Depression	-1.46	-4.07	-42.3	-16.7	0.309
Experimental yield	Depression	0.00	0.00	49.08	17.04	0.347
Simulation ultimate	Depression	-42.3	-16.7	-100	-24.9	0.142
Experimental ultimate	Depression	49.08	17.04	63.28	20.10	0.215

4.2.3 Translation Along AP Axis

Figure 4.7 displays the result of AP translation verification based on Spencer and Kuhn (2004). The figure compares the simulated results to experimental data extracted from Spencer and Kuhn (2004) in AP translation. The stiffness is calculated with Equation (2.2) and presented in Table 4.6. The results demonstrate close agreement between the simulated and experimental stiffness values, with only minor deviations observed.

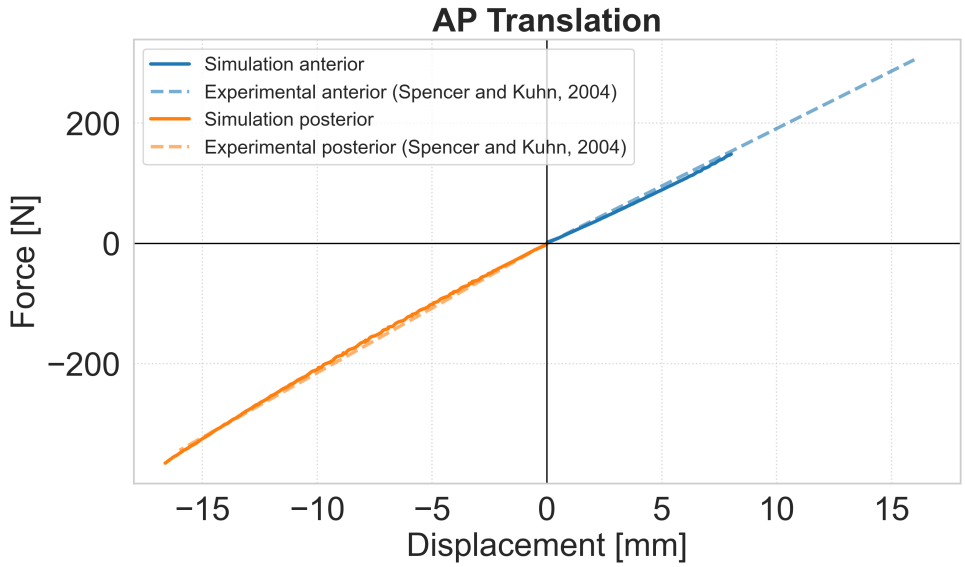

Figure 4.7: Comparison between simulated and experimental results in AP translation for the SC ligament. The experimental values were extracted from Table I and Table II in Spencer and Kuhn, 2004.

Table 4.6: Comparison of AP translational stiffness values obtained from experimental data from Spencer and Kuhn (2004) and simulation results. Simulation stiffness was calculated from the force–displacement response. The stiffness values for the Experimental were not calculated and were extracted from Spencer and Kuhn (2004).

Dataset	Dir	F_0 [N]	d_0 [mm]	F_1 [N]	d_1 [mm]	K [N/mm]
Experimental	Anterior	–	–	–	–	19.1
Simulation	Anterior	0.01	0.000	148.43	8.025	18.5
Experimental	Posterior	–	–	–	–	21.5
Simulation	Posterior	-0.01	0.000	-76.24	-3.797	20.1

4.3 Biomechanical Response Corridors

The construction of the biomechanical response corridors included data processing, PCA, Bayesian regression, and reconstruction of predicted response curves. Since the deflection data could not be used for the full analysis, the biomechanical response corridors were based on the force-time response.

4.3.1 Data Processing

The digitised force curves were interpolated to a common time grid. Figures 4.8a, 4.8c, 4.8e shows that the interpolated curves follow the digitised data points closely while providing a consistent representation across subjects and impact conditions. The deflection data was also processed initially, but as seen in Figures 4.8b, 4.8d, 4.8f, the common interpolation

interval became too short to capture peak deflection for several curves. Therefore, the remaining analysis was restricted to the force response.

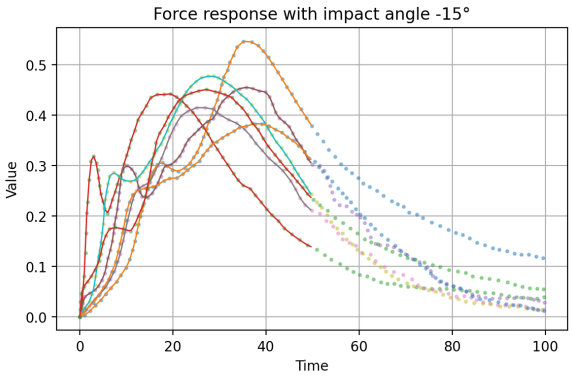

(a) Force −15°

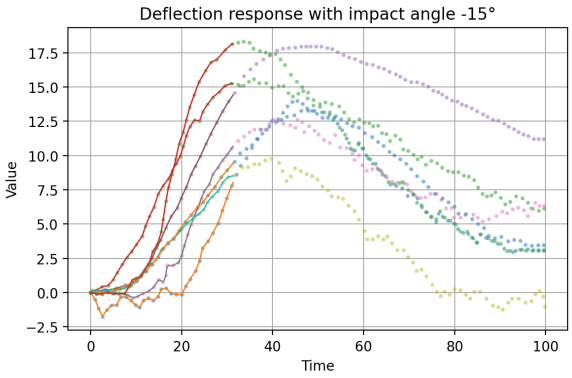

(b) Deflection −15°

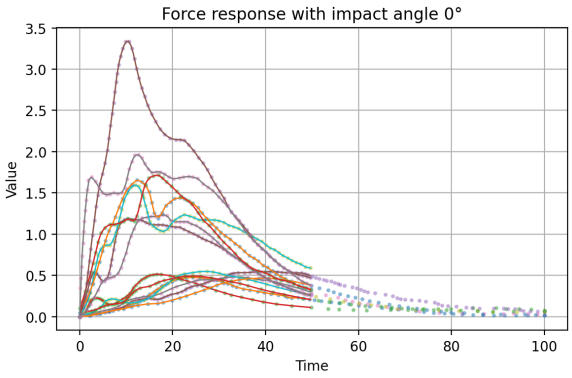

(c) Force 0°

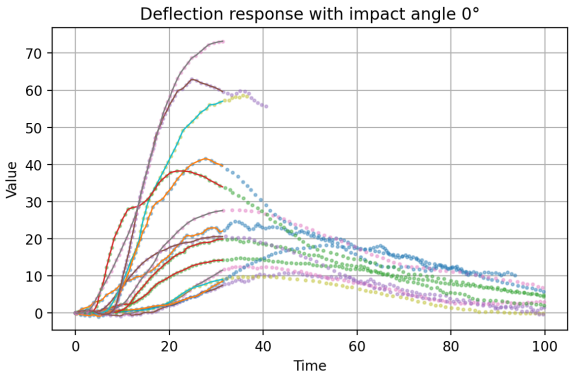

(d) Deflection 0°

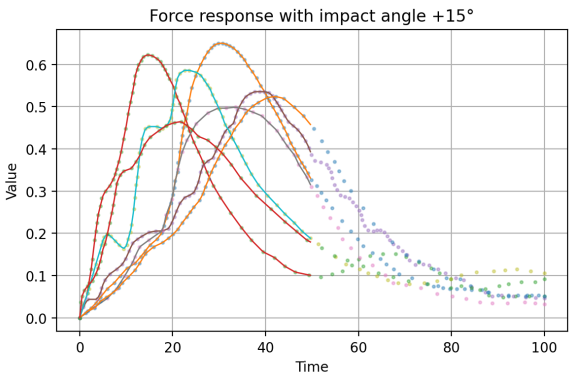

(e) Force 15°

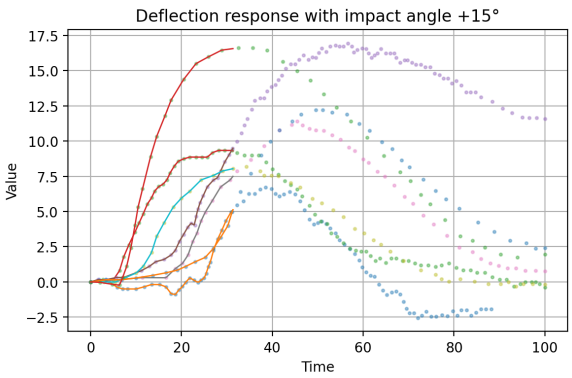

(f) Deflection 15°

Figure 4.8: Comparison between digitised and interpolated PMHS force and deflection curves for the three impact angles. The dotted lines represent the digitised data points, while the solid lines show the interpolated curves.

4.3.2 Principal Component Analysis

Figure 4.9 shows the individual and cumulative explained variance ratio for the principal components. The cumulative variance shows how much of the total variation is captured

when additional PCs are included. PC1–3 explained approximately 98% of the total variance, which means that most of the variation in the force-time curves could be represented by the first three PCs. Therefore, these components were selected for the regression analysis.

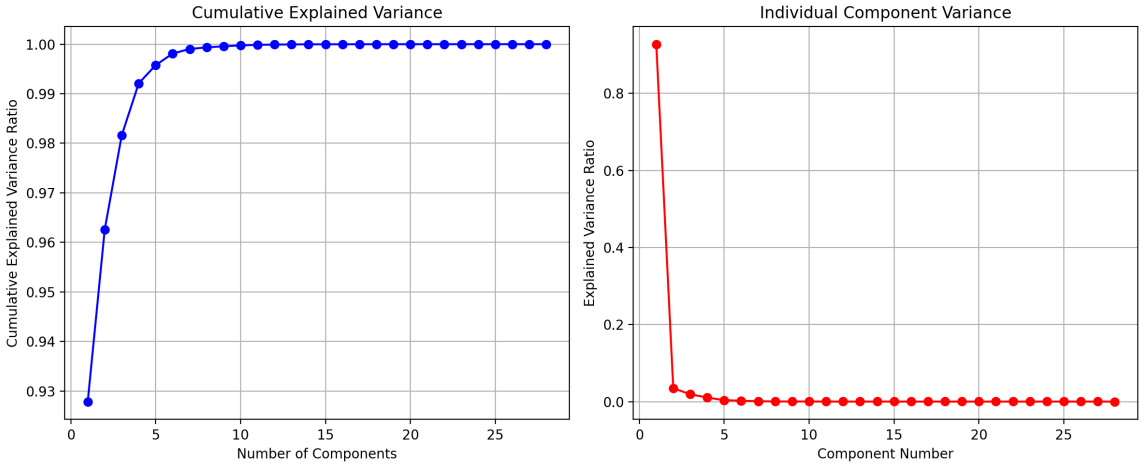

Figure 4.9: Explained variance ratio for the PCA of the force-time curves. The markers in the individual variance show how much each PC explains separately. While in the cumulative variance, the markers show how much total variance is captured as more PCs are included.

Figure 4.10 shows four different types of RMSEs between the original and reconstructed PC curves. Figure 4.10a shows that the total RMSE decreases rapidly until about 4 PCs, after that the slope starts to level off. Figure 4.10b shows that the error is large when only using the first PC, especially for subject 2. However, the error decreases fast and at three PCs the RMSE for all subjects are well below 0.1. The RMSE per angle in Figure 4.10c shows a similar behaviour. Figure 4.10d shows that the error for 6 m/s is exceedingly large for the first two PCs, but after that, the RMSE decreases rapidly. These observations supports the choice of three PCs.

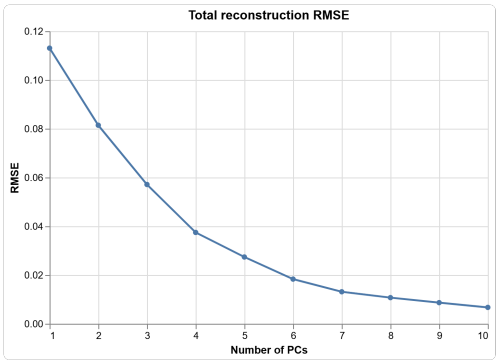

(a) Total reconstruction RMSE

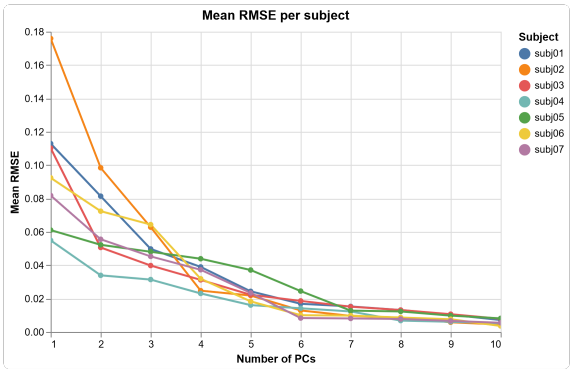

(b) Mean RMSE per subject

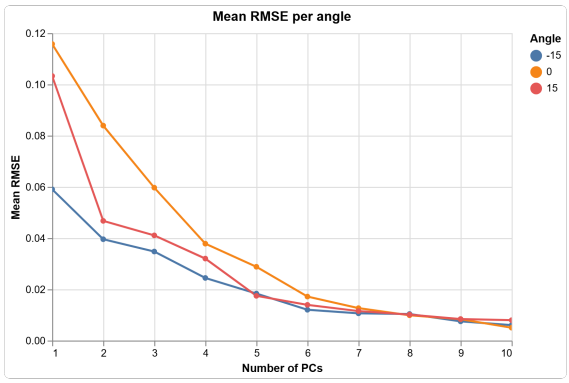

(c) Mean RMSE per angle

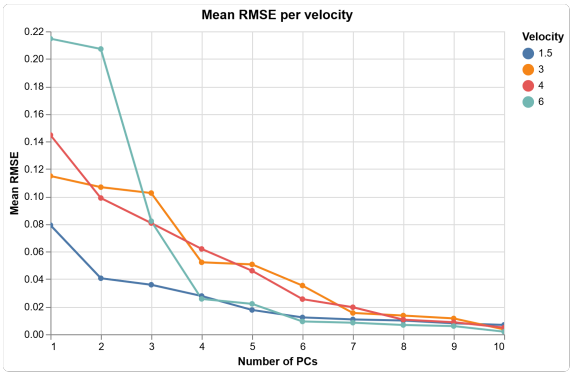

(d) Mean RMSE per velocity

Figure 4.10: Different types of RMSE illustrations of the difference between original and reconstructed PC curves.

Figure 4.11 shows PC1 score scattered against velocity, where PC1 increases with higher impact velocity.

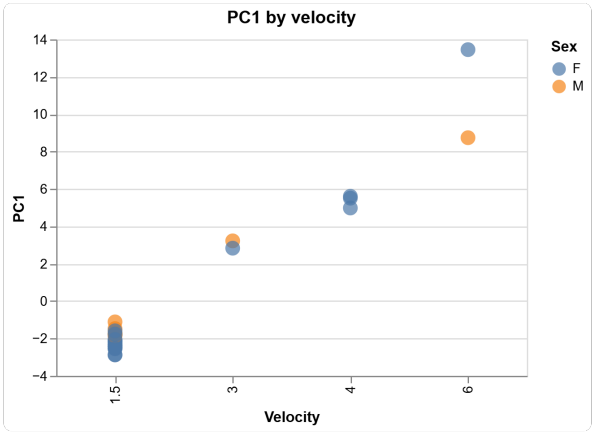

Figure 4.11: PC1 scores plotted against impact velocity.

Figure 4.12 shows the original curves and the reconstructed PCs separately. PC1 mainly captured global amplitude differences between the force curves, while PC2 and PC3 represented smaller variations of the curves, such as shape and timing.

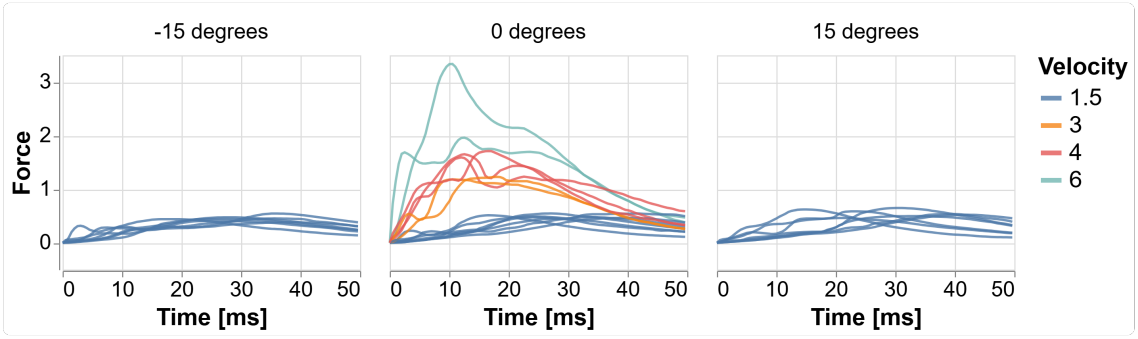

(a) Original curves

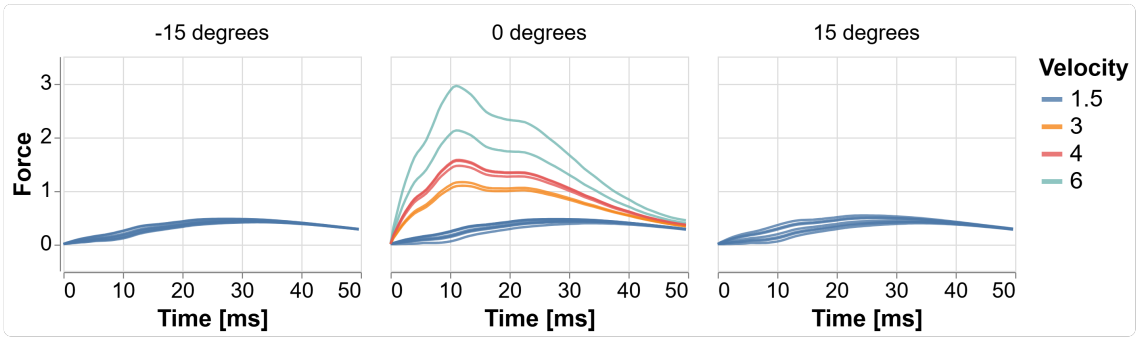

(b) PC1 reconstructions

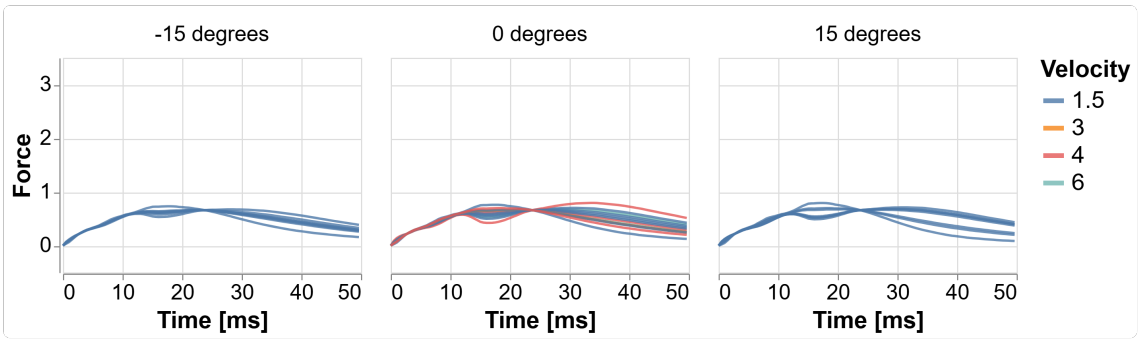

(c) PC2 reconstructions

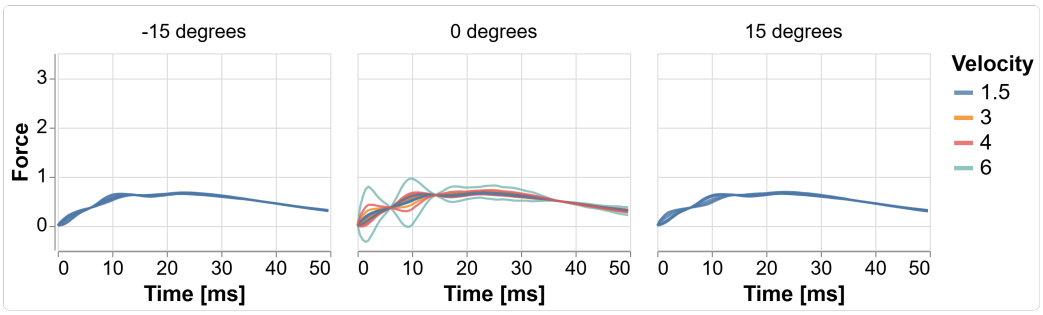

(d) PC3 reconstructions

Figure 4.12: Comparison between the original force-time curves and the reconstructed PC curves for different impact angles.

4.3.3 Bayesian Regression

Tables 4.7 - 4.9 summarises the LOO comparisons for PC1-3 respectively. In the rows, we have the compared models, and in the columns, we have:

- rank: The order of the models, from best to worst.
- elpd_loo: The ELPD value.
- elpd_diff: The difference between the ELPD for the highest ranked model.
- dse: The standard error of the differences.

Table 4.7 shows that the velocity model for PC1 obtained the highest elpd_loo. The models that include weight and flesh thickness had similar predictive performance and their elpd_diff relative to velocity are small compared to the corresponding uncertainty. while models excluding velocity performed substantially worse.

Table 4.7: LOO comparison of candidate Bayesian regression models for PC1.

Model	rank	elpd_loo	elpd_diff	dse
Velocity	0	-39.92	0.00	0.00
Velocity + weight	1	-40.19	0.27	1.33
Velocity + flesh thickness	2	-40.51	0.59	0.50
Velocity + sex	3	-41.40	1.48	1.00
Velocity + sex + flesh thickness	4	-42.54	2.63	1.47
Velocity + angle	5	-43.57	3.65	1.50
Angle	6	-80.03	40.12	6.67
Angle + sex	7	-81.23	41.31	6.77

Table 4.8 shows that the velocity + sex model has the highest elpd_loo but the elpd_diff between the highest ranked models are small relative to the uncertainty. Models that includes velocity generally perform better than models that includes angle.

Table 4.8: LOO comparison of candidate Bayesian regression models for PC2.

Model	rank	elpd_loo	elpd_diff	dse
Velocity + sex	0	-33.50	0.00	0.00
Velocity + sex + flesh thickness	1	-33.63	0.13	1.12
Velocity + weight	2	-33.96	0.46	0.66
Velocity	3	-34.10	0.60	0.76
Velocity + flesh thickness	4	-34.24	0.75	0.98
Angle	5	-34.75	1.25	1.91
Angle + sex	6	-34.81	1.31	1.62
Velocity + angle	7	-36.12	2.62	1.36

The angle + sex model was ranked highest, followed closely by the angle model. The angle + sex model showed poor sampling diagnostics, including 20 divergences. The angle model had similar predictive performance but no divergences and better sampling diagnostics.

Table 4.9: LOO comparison of candidate Bayesian regression models for PC3.

Model	rank	elpd_loo	elpd_diff	dse
Angle + sex	0	-29.74	0.00	0.00
Angle	1	-29.96	0.21	1.49
Velocity	2	-31.95	2.21	3.64
Velocity + sex	3	-32.11	2.37	2.86
Velocity + angle	4	-32.69	2.94	2.38
Velocity + sex + flesh thickness	5	-32.94	3.20	3.17
Velocity + weight	6	-33.70	3.95	3.52
Velocity + flesh thickness	7	-34.22	4.47	4.13

4.3.4 Construction of Corridors

Figure 4.13 shows the comparisons between using the posterior predictive samples and the posterior samples of the expected response. To keep this comparison constant, all figures use 95% HDI PC-space corridors. The mean responses are similar, but the posterior predictive corridors are wider than the expected response corridors.

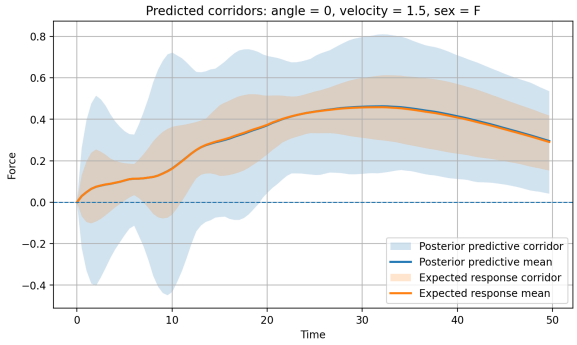

(a) Velocity 1.5 m/s

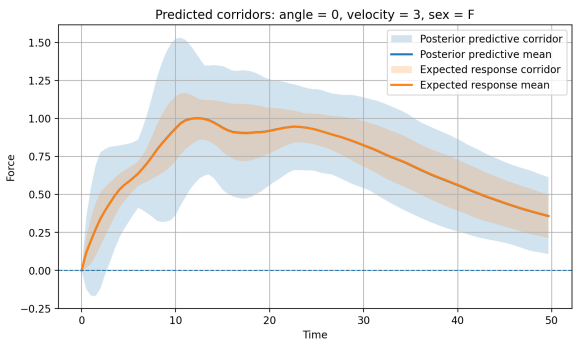

(b) Velocity 3 m/s

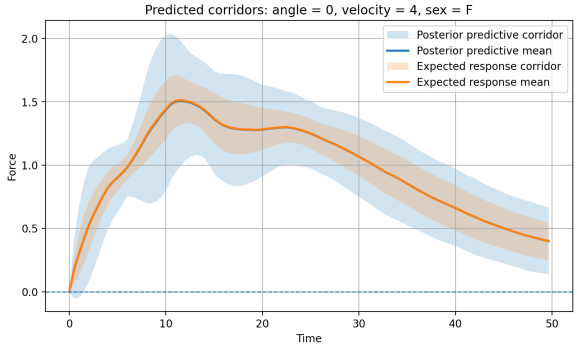

(c) Velocity 4 m/s

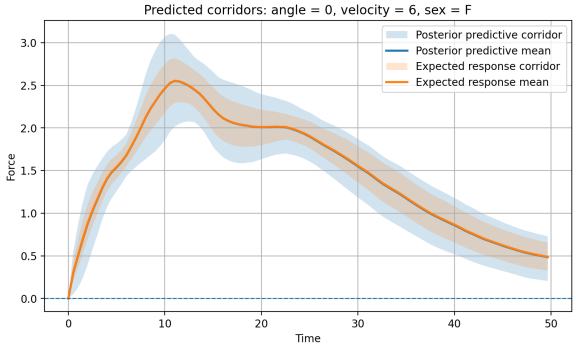

(d) Velocity 6 m/s

Figure 4.13: Comparison between corridors constructed from posterior predictive samples and posterior samples of the expected response for different impact velocities.

Figure 4.14 shows the comparisons between the PC-space method and the curve-space method. The mean curves are almost the same for both methods, but the corridor limits differ slightly between the PC-space and curve-space methods.

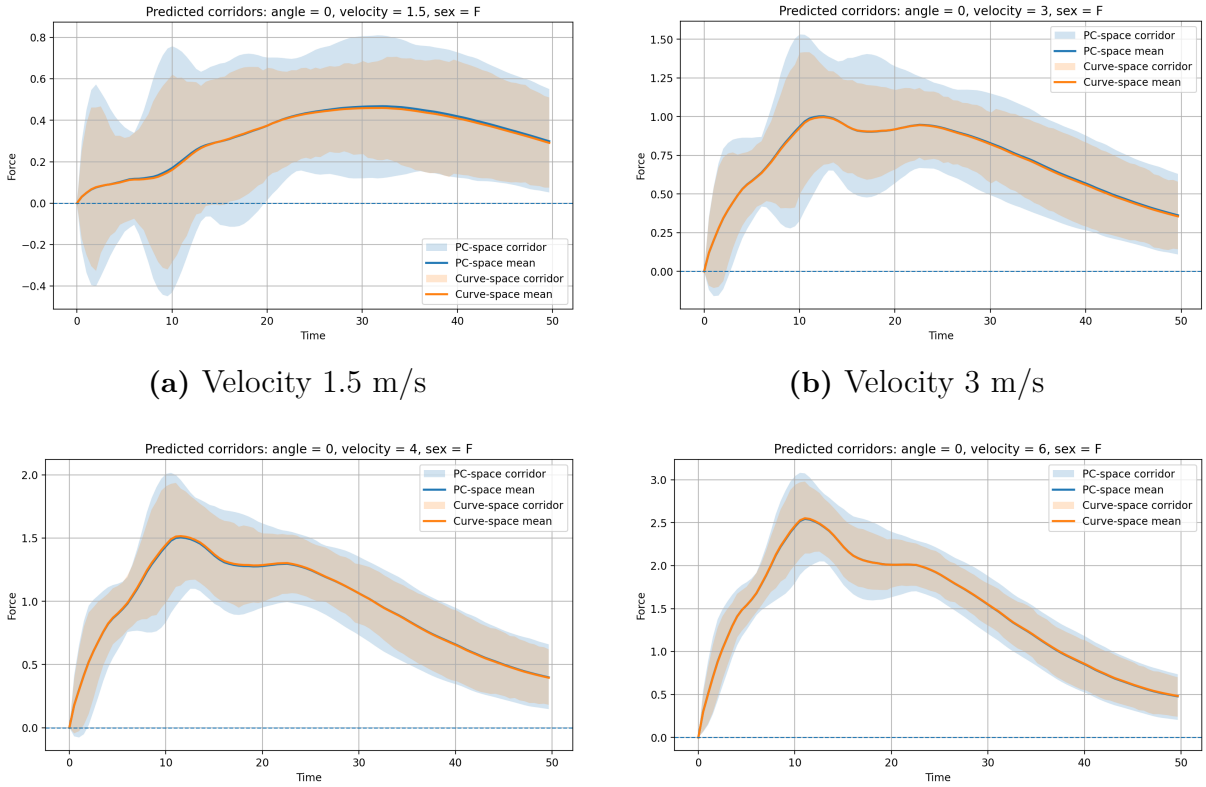

(a) Velocity 1.5 m/s

(b) Velocity 3 m/s

(c) Velocity 4 m/s

(d) Velocity 6 m/s

Figure 4.14: Comparison between corridors constructed in PC-space and curve-space for different impact velocities.

Figure 4.15 shows the difference between using two and three PCs in the corridor construction. Including an additional PC increases the variation in the corridors, since more information from the force-time curves is included. However, adding PC3 also affects the shape of the reconstructed corridors, especially in the early part of the response. This shows that the number of selected PCs influences both the width and the physical reasonability of the final corridors.

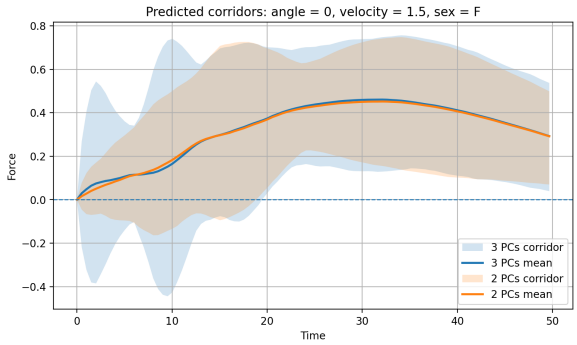

(a) Velocity 1.5 m/s

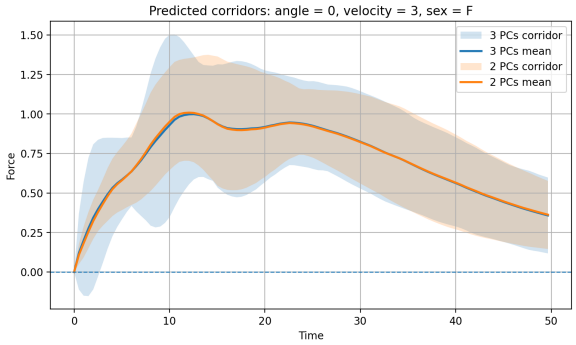

(b) Velocity 3 m/s

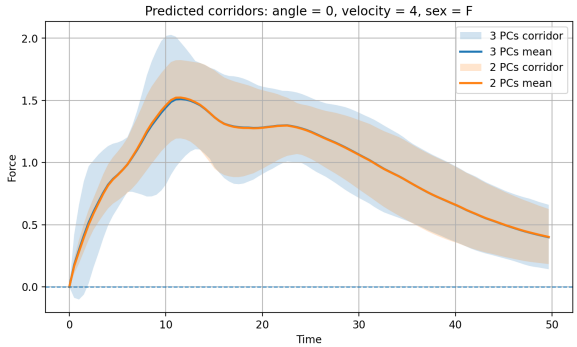

(c) Velocity 4 m/s

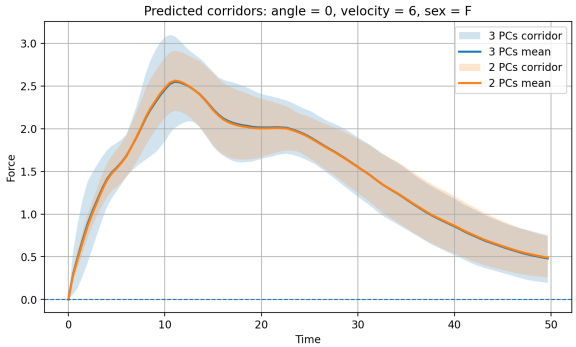

(d) Velocity 6 m/s

Figure 4.15: Comparison of corridors constructed using two and three PCs for different impact velocities.

Figure 4.16 shows the difference between using two and three PCs for different angles. The comparison illustrates how the selected number of PCs affects the corridor shape when the impact angle changes. Adding PC3 affects the shape of the reconstructed corridors, especially in the early part of the response.

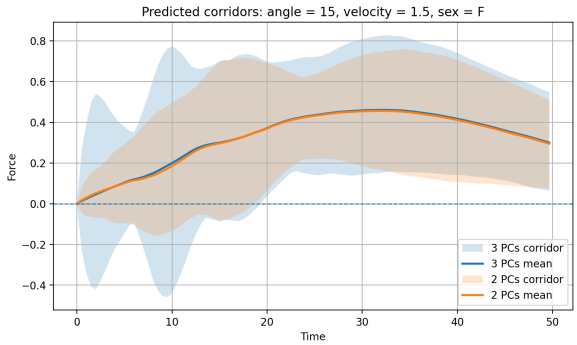

(a) Angle 15°

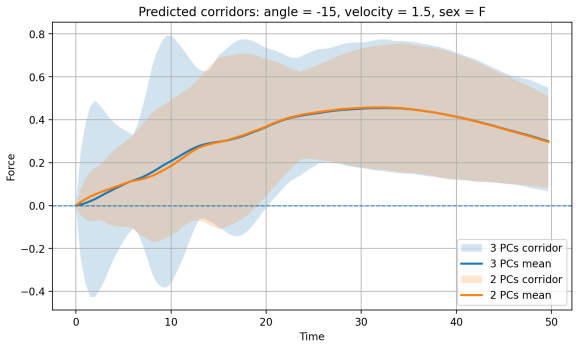

(b) Angle −15°

Figure 4.16: Comparison of corridors constructed for different impact angles using two and three PCs.

4.4 Full Body Simulation

The following section presents the results from the full body simulation made to replicate Compigne et al. (2004) at 0 degrees at three different velocities, 1.5 m/s, 3 m/s, and 6 m/s.

Figure 4.17a and Figure 4.17b represents the impactor force and deflection for the replicated Compigne et al. (2004) test at 1.5 m/s and 0 degrees. The figures includes experimental data from Compigne et al. (2004) and data from the old VIVA+, both downloaded from the VIVA+ repository (Kranjec, 2024), and the data from the VIVA+ with new AC and SC joints for both male and female. Figure 4.17c represents the force vs. deflection for the replicated Compigne et al. (2004) test at 1.5 m/s and 0 degrees. This figure includes data from the old VIVA+ downloaded from the VIVA+ repository (Kranjec, 2024) and the data from the VIVA+ with new AC and SC joints for both male and female. The figure also includes experimental data from Compigne et al. (2004). The VIVA+ with new AC and SC joints shows a softer response than the old VIVA+.

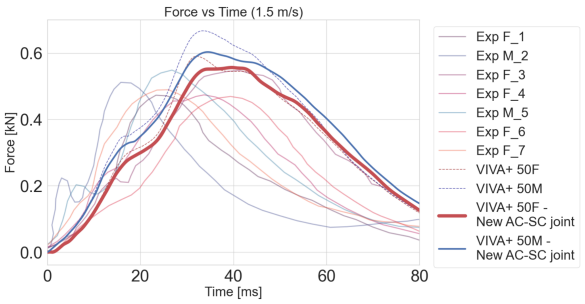

(a) Impactor Force 1.5 m/s

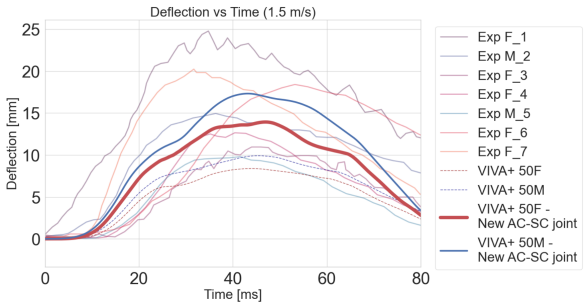

(b) Deflection (acromion to acromion) 1.5 m/s

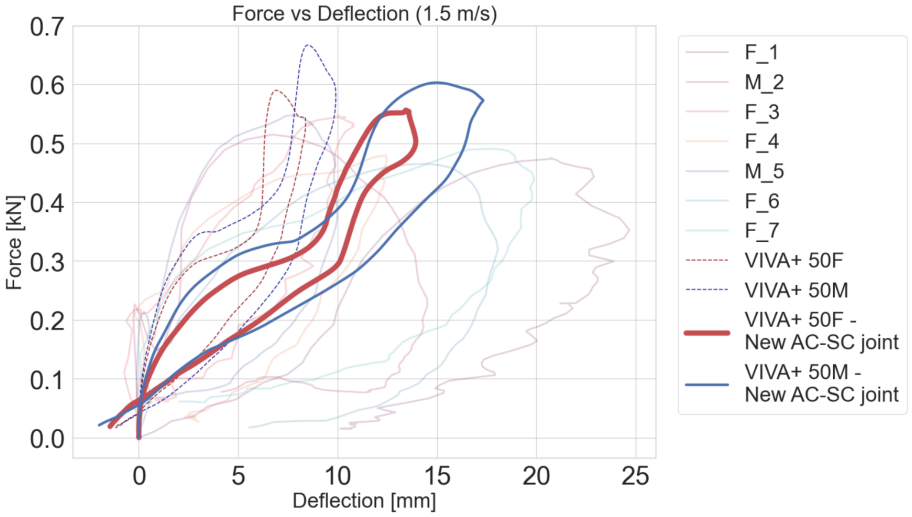

(c) Force vs. deflection (acromion to acromion) 1.5 m/s

Figure 4.17: Simulation results of impact test replicated from Compigne et al. (2004) at 1.5 m/s for male and female. a) Includes force vs. time results from the old VIVA+, results from the VIVA+ with new AC and SC joints for both male and female, and experimental data from Compigne et al. (2004). b) Includes deflection (acromion to acromion) vs. time results from the old VIVA+, results from the VIVA+ with new AC and SC joints for both male and female, and experimental data from Compigne et al. (2004). c) Includes force vs. deflection (acromion to acromion) results from the old VIVA+ and results from the VIVA+ with new AC and SC joints for both male and female, and experimental data from Compigne et al. (2004).

Figure 4.18 represents the impactor force, deflection force, and force vs. deflection for the replicated Compigne et al. (2004) test at 3 m/s and 0 degrees. All figures include data from the VIVA+ with new AC and SC joints for both male and female. The test for 3 m/s has no data available for the old VIVA+ model, therefore there is nothing to compare the new data to. The female shows a softer response compared to the male.

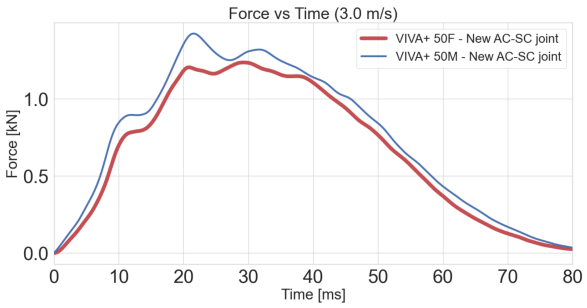

(a) Impactor Force 3 m/s

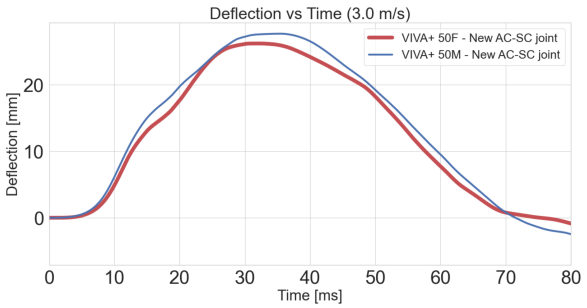

(b) Deflection (acromion to acromion) 3 m/s

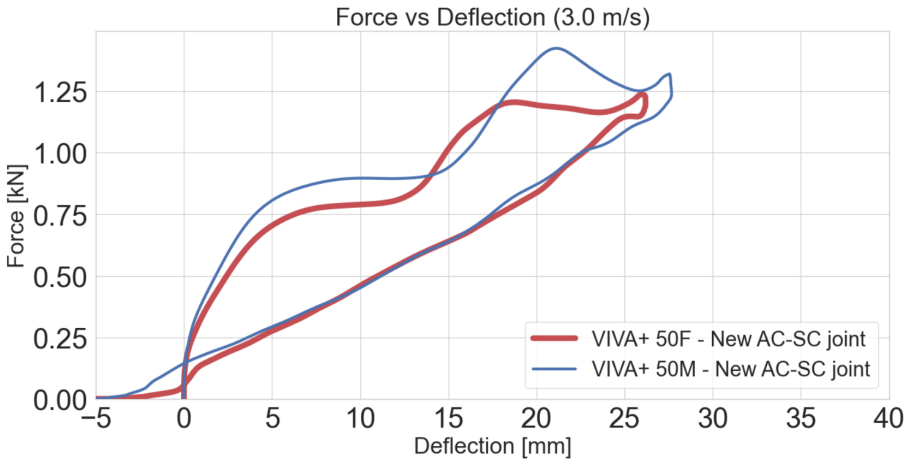

(c) Force vs. Deflection (acromion to acromion) 3 m/s

Figure 4.18: Simulation results of impact test replicated from Compigne et al. (2004) at 3 m/s for male and female. a) Includes force vs. time results from the VIVA+ with new AC and SC joints for both male and female. b) Includes deflection (acromion to acromion) vs. time results from the VIVA+ with new AC and SC joints for both male and female. c) Includes force vs. deflection (acromion to acromion) results from the VIVA+ with new AC and SC joints for both male and female.

Figure 4.19a and Figure 4.19b represents the impactor force and deflection for the replicated Compigne et al. (2004) test at 6 m/s and 0 degrees. The figures include data from the old VIVA+ downloaded from Kranjec (2024), and the data from the VIVA+ with new AC and SC joints for both male and female. Figure 4.19c represents the force vs. deflection for the replicated Compigne et al. (2004) test at 1.5 m/s and 0 degrees. This figure includes experimental data from Compigne et al. (2004) and data from the old VIVA+, both downloaded from the VIVA+ repository (Kranjec, 2024), and the data from the VIVA+ with new AC and SC joints for both male and female. The VIVA+ with new AC and SC joints shows a softer response than the old VIVA+.

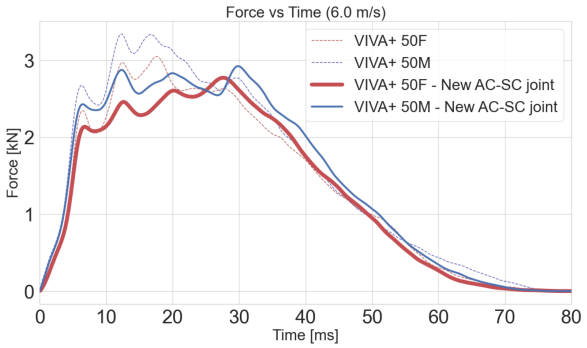

(a) Impactor Force 6 m/s

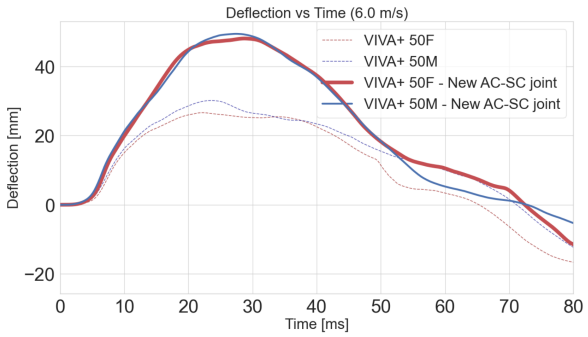

(b) Deflection (acromion to acromion) 6 m/s

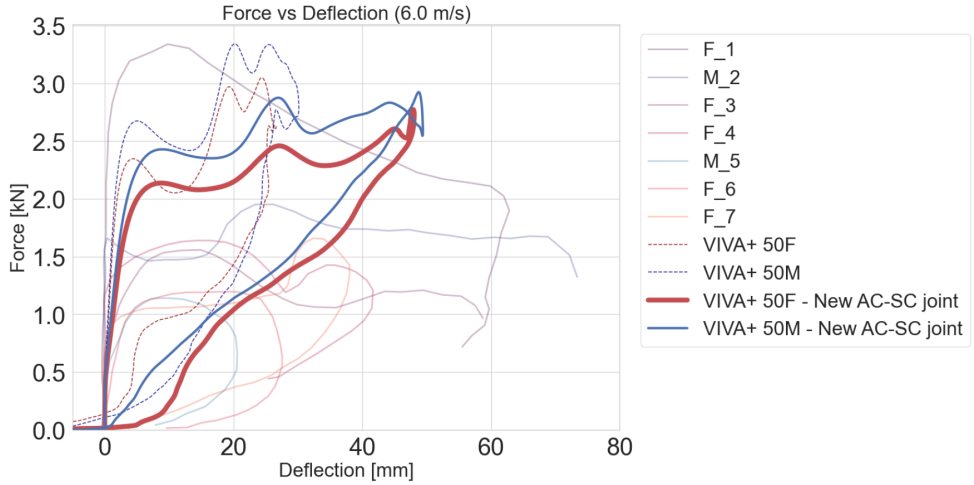

(c) Force vs. Deflection (acromion to acromion) 6 m/s

Figure 4.19: Simulation results of impact test replicated from Compigne et al. (2004) at 6 m/s for male and female. a) Includes force vs. time results from the old VIVA+ and results from the VIVA+ with new AC and SC joints for both male and female. b) Includes deflection (acromion to acromion) vs. time results from the old VIVA+ and results from the VIVA+ with new AC and SC joints for both male and female. c) Includes force vs. deflection (acromion to acromion) results from the old VIVA+, results from the VIVA+ with new AC and SC joints for both male and female, and experimental data from Compigne et al. (2004)

4.4.1 Comparison of New Model with Corridors

In Figures 4.20 - 4.22 the force-time curves for all six cases, female and male at velocities 1.5 m/s, 3 m/s, and 6 m/s, are plotted together with the created corridors. All figures include the created corridor for the specific case and the data from the VIVA+ with the new AC and SC joint. Figure 4.20a shows that the VIVA+ with new AC and SC joints are within the span of the corridor. Figure 4.20b are also somewhat within the corridor, although the end of the curve extends slightly outside. In Figure 4.21 both plots are to some extent within the corridors, but most of the curves is outside of it. Also for Figure 4.22 both curves is mostly outside of the corridors. The curve that shows results most within the corridors is the female for 1.5 m/s.

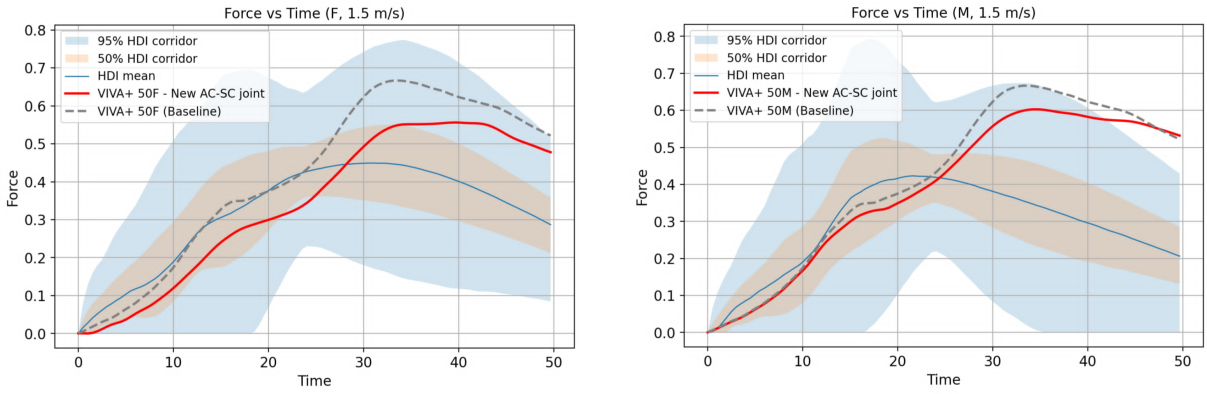

(a) Female 1.5 m/s **(b)** Male 1.5 m/s

Figure 4.20: Comparison of corridor and new VIVA+ model when impacting in 1.5 m/s

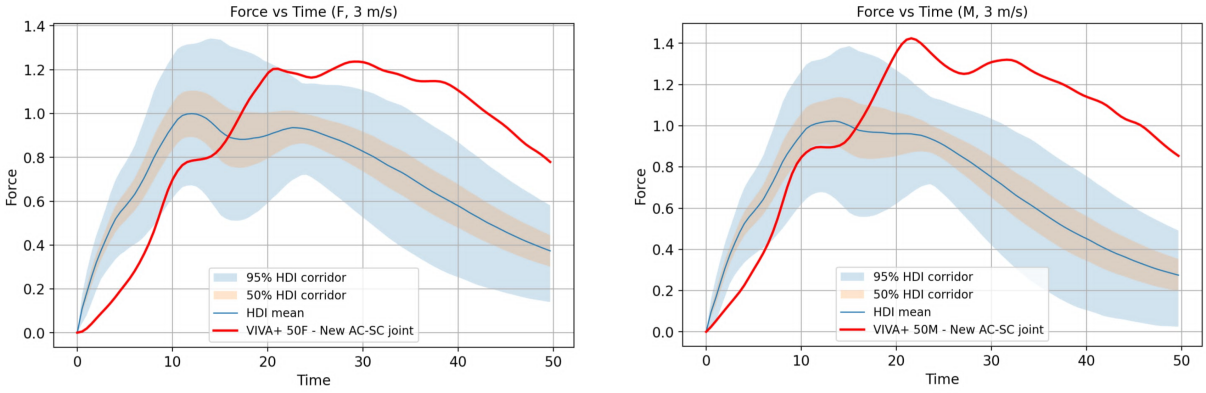

(a) Female 3 m/s **(b)** Male 3 m/s

Figure 4.21: Comparison of corridor and new VIVA+ model when impacting in 3 m/s

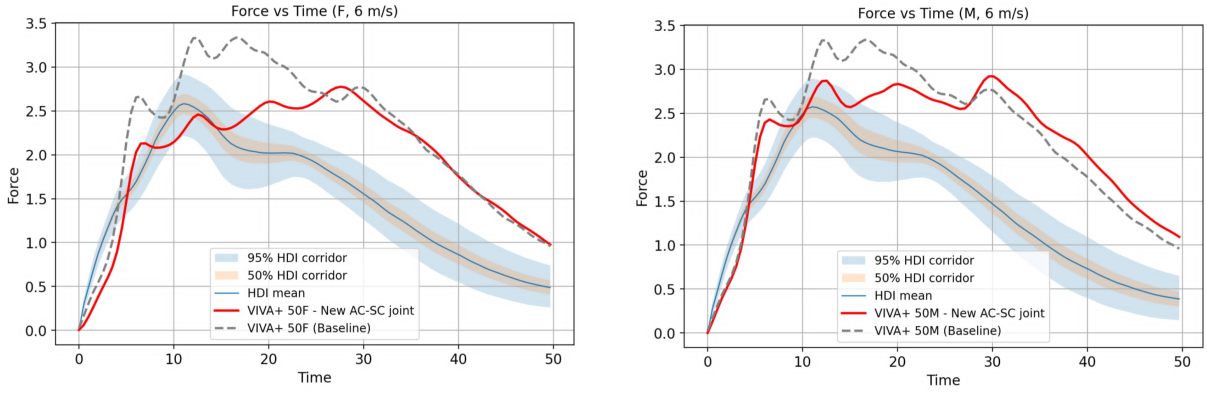

(a) Female 6 m/s **(b)** Male 6 m/s

Figure 4.22: Comparison of corridor and new VIVA+ model when impacting in 6 m/s

5

Discussion

During this project, two joints were implemented, and biomechanical response corridors were constructed. In this chapter the methods and outcomes from this project are discussed.

5.1 Implementation of Load Curves

The verification simulations indicates that the curves are successfully implemented. Even if the curves not always matches the experiments perfectly, for most of the cases the stiffnesses, i.e. the calculated K value, is comparable.

However, a recurring issue throughout the verification of the load curves for both AC and SC joints is the initial spike of force in the simulations, that the experiments do not have. The reason that has not been ruled out, is that a fast acceleration causes inertial effects. In some of the articles a force was presented rather than a velocity. Despite this, a velocity was applied in LS-DYNA. Because of this the velocity had to be approximated and adjusted to obtain a force close to the desired one. Nevertheless, since the initial force spike is a recurring problem for almost all curves, it does not seem that applying the velocity instead of a force is the issue. One possible solution to avoid the initial spike could be a slower ramp-up to the velocity together with a longer simulation time. That would probably lead to a better result, but due to limited computational capacity this was not implemented and tested. Another solution to avoid the initial spike could be to apply a minimal force before the given force. This type of force was applied in Koh et al. (2004), where it was used to overcome inertial effects that often occur at the beginning of the test, as in this simulated test. When the small force was applied before the other force, the machine had time to accelerate to a constant speed before the ligament actually began to stretch.

Another issue to why the curves do not match exactly could be that the information from the literature was presented differently across studies. In some studies, the aim was to find the yield point and the breaking point, while in others, it was presented as a much more detailed force-deflection curve. Further, some studies only state a stiffness value, with

the force or displacement calculated based on that value, which provides only one point. When verifying the load curve against the simulation results, this needs to be taken into account, since the curves do not appear similar. Hence, the stiffnesses were calculated to compare the curves more effectively. Another aspect that could affect the result is that not all load curves are based on literature; some are estimated. A more developed model could investigate these DOFs, which would likely improve the results.

A further problem when implementing information from the literature in LS-DYNA was how to interpret it correctly. Sometimes the needed information to insert them into LS-DYNA was missing or could be misinterpreted. For example, where the beam should be placed in the model was determined solely by trying to replicate the anatomy of the shoulder. Furthermore, sometimes the original model of the shoulder in LS-DYNA did not match the anatomy described in the literature exactly. This is because the model of the shoulder in LS-DYNA is simplified compared to true human anatomy. Additionally, it was sometimes difficult to understand from where in the model displacements and forces were supposed to be measured from, or where the rotation centre was supposed to be. This could affect the values even if the implementation of the load curve was correct.

Another example of this, where there was a difference between the simulated and real test was in the PMHS test made by Negri et al. (2014). The ligaments from the test subjects were attached with screws to the machine. This meant that the ligament was considered fully constrained but it might still move slightly, which could affect the results. When simulating this loadcase in LS-DYNA, the ligament was fully constrained and could not move at all. This leads to the displacement probably differentiating somewhat between the simulation and the test. For other tests where DOFs was constrained this problem occurred as well, and need to be considered in the results.

The load curves in ML-translation, for both SC and AC joint and SI translation for SC (see Figures 3.7, 3.8 and 3.9), were modified by removing the unloading part after the first simulation of Compigne et al. (2004) validation. A comparison of the simulation results indicated that the version without the unloading part was more biofidelic. The unloading part represents the moment when the ligament begins to tear. In the simulation including the unloading part, the failure part of the ligaments will be simulated, however the focus should remain on the behaviour leading up to failure, since VIVA+ does not model for failure. By removing the unloading part, the ligament will not model for any failure behaviour. After reaching the maximum displacement of the load curve, the subsequent behaviour is uncertain. The displacement will most certainly continue beyond the maximum value specified in the load curve, since this has been observed multiple times in the verification models. It is unclear what happens to the force required to continue

beyond the maximum displacement, but it is hypothesised that it continues in the tangent direction of the last data point in the load curve. If this is the case it suggests that in the simulation with the unloading part still there, the force will continue towards zero and negative values. With the assumption from above and the unloading part removed the force and deflection will continue in the tangent direction to eternity. Gaining a deeper understanding of this behaviour could facilitate a more accurate implementation of load curves, ultimately leading to a more biofidelic model of the shoulder.

5.2 Interpretation of Principal Components

As shown in Figure 4.9, the first three PCs explain more than 98% of the total variance and are therefore the focus of the analysis.

5.2.1 PC1

Figure 4.12b shows that PC1 primarily captures global amplitude differences between the curves, representing the overall response level rather than local shape variations. PC1 also appears strongly related to impact velocity, as higher velocities correspond to higher PC1 scores in Figure 4.11. This suggests that velocity accounts for a large portion of the variation in the dataset.

PC1 also reflects differences between impact angles. The responses at 0° show a larger spread and generally higher amplitudes than those at ±15°. However, since the 0° condition includes several impact velocities, the influence of angle cannot be separated from the influence of velocity.

5.2.2 PC2

Figure 4.12c indicates that PC2 captures differences in curve shape and timing rather than overall amplitude. The component appears to describe variation in peak timing, pleteau location and post-peak decay.

Some curves exhibit an early peak at 10-20 ms, while others peak around 30 ms, suggesting that PC2 represents differences in how quickly the response develops. These variations may be related to impact velocity as well as subject-specific characteristics such as sex, weight or flesh thickness. Softer or larger tissue volumes may produce broader and delayed responses, while stiffer or smaller tissue volumes may lead to sharper and earlier responses.

5.2.3 PC3

Figure 4.12d suggests that PC3 captures local shape variations, particularly during the early stage of the response. The component therefore appears to describe aspects of the

initial impact behaviour.

As for PC2, the observed variation may be influenced by both impact conditions, such as velocity and angle, and subject-specific characteristics related to softness or structure.

5.3 Bayesian Model Comparison and Feature Effects

The model comparisons in Tables 4.7-4.9 indicates that different predictors are relevant for different PCs, which is expected since the components describe different aspects of the force curve.

For PC1, models including velocity performed substantially better than the models based on angle. This is consistent with the PC interpretation, where PC1 mainly captured the global amplitude differences and was strongly related to velocity. Since the impact velocity directly affects the energy and load at impact, it is physically reasonable that it explains a large part of the variation in PC1.

For PC2, the highest ranked model included sex but several models showed similar predictive performance. Therefore, this should not be interpreted as strong evidence of isolated sex effect. Instead, PC2 may capture subject-related differences in curve shape or timing that are only partly explained by the available predictors.

For PC3, the relationship to impact angle appeared stronger than for PC1 and PC2. However, the improvement from adding sex was not considered reliable due to sampling issues in the angle + sex model. The selected angle model should therefore be interpreted as a more stable and cautious choice for corridor construction.

All selected models showed acceptable sampling diagnostics, with no divergences and a maximum R-hat of 1.01. Pareto-k warnings occurred in all LOO comparisons and were consistently associated with the 6 m/s data. This suggests that the highest velocity impacts behave differently from the rest of the datasets, which is reasonable given their substantially higher force levels. The LOO ranking should therefore be interpreted with caution, particularly when assessing model performance for high velocity impacts.

5.4 Corridor Construction and Quality

Since the shape and width of the final corridors depend on several modelling choices, the quality of the corridors was evaluated by comparing different ways of representing uncertainty, constructing the intervals, and selecting the number of PCs. This helps clarify

how the corridors should be interpreted when comparing them with the VIVA+ model response.

5.4.1 Posterior Predictive and Expected Response

Figure 4.13 shows that the mean response curves are very similar for all scenarios. The choice of distribution therefore has little effect on the central prediction and mainly influences the corridor width, which represents uncertainty. As expected, the posterior predictive distributions produce wider corridors because they include the residual variation associated with new observations. They are therefore more suitable for comparison with HBM simulations, which represent individual responses rather than population means.

The differences are largest at low velocity, as shown in Figure 4.13a. Here, the posterior predictive corridors are substantially wider and extend below zero at the beginning of the response. This effect becomes smaller or disappears at higher velocities, where the force level is larger relative to the uncertainty. The result suggests that variation in PC space can generate curve shapes that are statistically plausible within the model but not always physically meaningful. In particular, the model does not enforce the physical constraint that contact force must be non-negative. Since negative contact force is non-physical, the lower bound of the final force corridors can be truncated at zero.

5.4.2 PC-Space and Curve-Space

Figure 4.14 shows that the PC-space and curve-space methods produce almost identical mean curves. The choice of method therefore has little effect on the predicted response itself and mainly influences how uncertainty is represented.

The PC-space corridors are slightly wider, particularly for the low-velocity scenario shown in Figure 4.14a. This may result from the use of envelope intervals on reconstructed curves, where a single extreme reconstruction can determine the corridor boundary. The differences become smaller at higher velocities, suggesting either that the posterior reconstructions are more concentrated or that the sampled PC scores generate fewer extreme shape variations. The limited amount of data may also contribute. Since only two PMHS were available for the 6 m/s condition, the estimated corridor is sensitive to the characteristics of those individuals and may not fully represent the variability of a larger population.

The two methods also differ in their statistical interpretation. In the PC-space approach, HDI bounds are computed independently for each PC score. These intervals therefore represent marginal HDIs for the individual components rather than a joint 95% credible region in the full PC space. For three PCs, three independent 95% intervals correspond to a joint coverage of approximately $0.95^3 \approx 0.86$. The reconstructed corridor should

therefore not be interpreted as an exact 95% credible region for the full response curve. In the curve-space approach, HDI bounds are instead computed independently at each time point after reconstruction. This makes the corridor easy to interpret in the time domain, but the resulting bounds do not necessarily correspond to physically realisable curves.

Since the regression models predict responses in PC space, the PC-space corridor is selected as the final method. This approach is directly linked to the uncertainty in the predicted PC scores, although it does not provide pointwise HDI bounds in the time domain.

5.4.3 Influence of Selected Principal Components

Figure 4.15 shows that the number of selected PCs has a clear effect on the response corridors. Although including PC3 increased the variance, the resulting corridors were less physically realistic than those based on PC1 and PC2 alone. As discussed previously, PC1 mainly represents overall amplitude differences, while PC2 captures variation in response shape and timing. In contrast, PC3 introduces local variation in the early response, including oscillatory behaviour and negative values at the beginning of the curve.

Since impact angle may influence the initial contact phase, an angle related component could reasonably affect the early response. However, the effect of PC3 was not expressed as a stable change in amplitude or timing. Instead, it mainly introduced additional shape variation that reduced the physical interpretability of the corridors. Because angle is only included in the regression model for PC3, excluding this component means that the final corridors depend only on velocity and sex. Figure 4.16 shows only marginal differences between the angle-specific corridors, suggesting that the angle effect is weak or not adequately captured by the current approach. The final corridors are therefore based on PC1 and PC2, representing a compromise between preserving variance and maintaining physical interpretability. This interpretation is supported by single PC corridors shown in Figure A.1, where PC3 mainly added noise and uncertainty rather than a clearly interpretable change in response shape.

5.5 Biofidelity in VIVA+ Model

When comparing the force-time curves from the new VIVA+ model with the created corridors, the results are better at low speed. In Figure 4.20 the low speed tests of 1.5 m/s are plotted. These are within the corridors for almost the entire simulation. For 3 m/s and 6 m/s the curves are in the corridors in the beginning of the simulation. The load curves for the ligaments are created with properties from tests performed with quasi-static velocities, therefore they can better represent the joints' behaviours at low velocities. Because the corridors were created based on few PMHS in both the 3 m/s and 6 m/s they are narrow,

see Figures 4.21 and 4.22, this means that even if the simulation seems to be far from the corridors it could still be a good result. For the simulation with velocity 3 m/s no prior data was available so the results could only be compared with the corridors and between the male and female models. This means that there is not any possibility to see if the VIVA+ with the new AC and SC joints was improved for this velocity, this because there is no baseline to compare with.

For all three simulations, the simulated data are close to the corridors at the beginning of the simulation in all of the cases, which was illustrated in Figure 4.20, 4.21 and, 4.22 However, as time passes, the simulated data become increasingly distant from the corridors. This could be because the load curves are based on ligaments that did not break. Because of this, as time goes on, the ligaments would break, but this was not simulated. In reality, in some of the cases, the bones would break as well (Compigne et al., 2004); this was not simulated either. It is possible in LS-DYNA to model with a failure flag, i.e. an element that is removed when the stress becomes too high. Even if it would be interesting to see the difference in results if a failure flag was used, what happens late in the simulation could be argued to not be as much of interest as the earlier stages of impact. This because it is more of interest to identify when damage starts to occur to prevent injuries.

The VIVA+ impact simulations with the new AC and SC joints show that the joints are less stiff compared to the previous AC and SC joints, and the results are more biofidelic. The acromion to acromion deflection is larger, compared to the old VIVA+ implementation, and the force deflection curve shows that there is more deflection with less force. This proves that the model response improved after the changes. The difference between the current joints and the new joints is that the new joints can move in six DOFs, while the previous implementation can move in all rotational DOFs but not in the translational DOFs. This is probably one important reason to why the new response is less stiff. However, the model is still too stiff compared to data from the PMHS in the Compigne et al. (2004) test. This indicates that the AC and SC joints only slightly effect the model, and it would possibly become better if the glenohumeral joint implementation was also investigated and updated according to literature.

The purpose of HBMs is to simulate and study how the human body responds to external loads, often in traffic safety. The joints that are created in this project are based on PMHS data. The validation case from Compigne et al. (2004) is also based on PMHS data and therefore the simulation is comparable. However, it is important to know that these results are based on PMHS and do not respresent the biomechanical response of a living human. There are several reasons that the response differ. One of these is that a living human can brace which should make the response stiffer. Another one is that PMHS tissue could be

stiffer due to rigor mortis. Since it is unethical to test on living human beings, there is no data to compare the differences in the responses. Therefore it is important to keep this in mind to interpret the results correctly.

5.6 Limitations of the Analysis

In addition to the project limitations stated in the introduction, there are other limitations that affect the modelling and simulation results, and the interpretation of the constructed corridors.

When creating the load curves for both AC and SC joints stiffnesses or other properties that could be used was not found in literature for all six DOFs. Therefore several load curves had to be approximated since their contribution to the shoulder joints is not known. Since the impact test is in the lateral direction and the ML load curve for the SC joint is approximated this probably affects the results from the simulations significantly.

Another limitation is that the experimental data was limited, with seven PMHS and four tests, where only one test covered the higher velocity range. The PMHS group was also limited, partly because there are few PMHS but also because they are old and short, and therefore do not represent a broad population. This restricts how generally the corridors can be interpreted. Also, some tests contained a small number of curves, which leads to uncertainty in the scenario-specific regression models and corridors.

Additionally, the deflection data had to be excluded, leaving the final corridors to describe only the impact force response and not the entire biomechanical response.

Moreover, the PCA-based regression and reconstruction framework imposes no constraints regarding physical plausibility, such as non-negativity of forces. This became clear when the corridors gave negative lower bounds for low velocities. Therefore, the corridors should be interpreted as model-based approximations of the experiments, rather than exact physical boundaries.

6

Conclusion

The intention of this thesis, was to create a more biofidelic shoulder joint for the VIVA+ model. This was achieved to some extent. Although the shoulder response from the lateral impact test from Compigne et al. (2004) does not match the PMHS tests perfectly, it is less stiff than in the previous implementation. The AC and SC joints are created based on literature and better replicate the mechanical behaviour of a real shoulder, even if the difference is small. The obtained results indicate that implementation of a more biofidelic glenohumeral joint has a high potential to improve the mechanical response of the shoulder joint under the impact test. However, further development is still needed, especially since the response did not fully match the experimental PMHS data.

Another objective was to identify the method that obtained the most well described corridors. This was done through comparisons of the different approaches for constructing biomechanical response corridors. It became evident that the posterior predictive PC-space corridors based on the first two PCs obtained the most well described corridors.

The corridors were created from experimental PMHS data and used as a comparison for the simulated shoulder response. By plotting the new VIVA+ results together with the corridors, the model could be compared with the expected range of human shoulder response. The comparison showed that the new AC and SC joint implementation made the shoulder response less stiff than before. However, the simulated response was still not fully within the biomechanical response corridors. This shows that the model has improved, but that further work is still needed to make the shoulder response more biofidelic.

Bibliography

Abril-Pla, O., Andreani, V., Carroll, C., Dong, L., Fonnesbeck, C. J., Kochurov, M., Kumar, R., Lao, J., Luhmann, C. C., Martin, O. A., Osthege, M., Vieira, R., Wiecki, T., & Zinkov, R. (2023). PyMC: a modern, and comprehensive probabilistic programming framework in Python. *PeerJ Computer Science*, *9*(e1516). https://doi.org/10.7717/peerj-cs.1516

Ansys Inc. (2023). General. Ansys LS-DYNA. https://lsdyna.ansys.com/knowledge-base/general/

Avani, R. (2024, December). Joint Identification Computer Vision Model. [Picture]. Universe. https://universe.roboflow.com/avani-rane-5gwdn/joint-identification-b0cya/images/82lWXAnJe4sQ3loIiU3K?queryText=&pageSize=50&startingIndex=0&browseQuery=true

Balderes, T. (2026, January). Finite element method. AccessScience. Retrieved March 22, 2026. https://doi.org/10.1036/1097-8542.257700

Barczak, T. M. (2017). Research developments that contributed to the landscape of longwall roof support design over the past 25 years. In *Advances in coal mine ground control* (pp. 1–34). Elsevier. https://doi.org/10.1016/B978-0-08-101225-3.00001-3

Beeman, S. M., Kemper, A. R., Madigan, M. L., Franck, C. T., & Loftus, S. C. (2012). Occupant kinematics in low-speed frontal sled tests: Human volunteers, Hybrid III ATD, and PMHS. *Accident Analysis & Prevention*, *47*, 128–139. https://doi.org/10.1016/J.AAP.2012.01.016

Bergh, D. v. d., Clyde, M. A., Gupta, A. R. N., de Jong, T., Gronau, Q. F., Marsman, M., Ly, A., & Wagenmakers, E. J. (2021). A tutorial on Bayesian multi-model linear regression with BAS and JASP. *Behavior Research Methods*, *53*(6), 2351–2371. https://doi.org/10.3758/s13428-021-01552-2

Capretto, T., Piho, C., Kumar, R., Westfall, J., Yarkoni, T., & Martin, O. A. (2022). Bambi: A Simple Interface for Fitting Bayesian Linear Models in Python. *Journal of Statistical Software*, *103*(15), 1–29. https://doi.org/10.18637/jss.v103.i15

Compigne, S., Caire, Y., Quesnel, T., & Verries, J.-P. (2004). Non-Injurious and Injurious Impact Response of the Human Shoulder Three Dimensional Analysis of Kinematics and Determination of Injury Threshold. *Stapp Car Crash Journal*, *48*, 89–123. https://doi.org/https://doi.org/10.4271/2004-22-0005

Dawson, P. A., Adamson, G. J., Pink, M. M., Kornswiet, M., Lin, S., Shankwiler, J. A., & Lee, T. Q. (2009). Relative contribution of acromioclavicular joint capsule and coracoclavicular ligaments to acromioclavicular stability. *Journal of Shoulder and Elbow Surgery*, *18*(2), 237–244. https://doi.org/10.1016/j.jse.2008.08.003

Devane, K., Hsu, F. C., Koya, B., Davis, M., Weaver, A. A., Scott Gayzik, F., & Guleyupoglu, B. (2023). Assessment of finite element human body and ATD models in estimating injury risk in far-side impacts using field-based injury risk. *Accident Analysis & Prevention*, *192*, 107274. https://doi.org/10.1016/J.AAP.2023.107274

Douglas, C. A., Fildes, B. N., Gibson, T. J., Boström, O., & Pintar, F. A. (2007). Factors influencing occupant-to-seat belt interaction in far-side crashes. *Annual proceedings. Association for the Advancement of Automotive Medicine*, *51*, 320–339. https://www.scopus.com/inward/record.uri?eid=2-s2.0-44849100927&partnerID=40&md5=48045ac2f616389acf96e47022bde893

Drake, R. L., Vogl, W., Mitchell, A. W. M., & Gray, H. (2015). *Gray's anatomy for students* (3rd ed.). Churchill Livingstone/Elsevier.

DYNAmore GmbH. (2026). Discrete Beam. LS-DYNA Support. Retrieved March 25. https://www.dynasupport.com/howtos/element/discrete-beam

Engineering Technology. (2026). Yield Strength. https://engineeringtechnology.org/engineering-materials/mechanical-properties-of-materials/strength/stress-strain-diagram/yield-strength/

Fahse, N., Millard, M., Kempter, F., Maier, S., Roller, M., & Fehr, J. (2023). Dynamic human body models in vehicle safety: An overview. *GAMM Mitteilungen*, *46*(2). https://doi.org/10.1002/gamm.202300007

Flores, C., Celik, H., Hoenecke, H., & D'Lima, D. D. (2023). Subject-specific computational modeling of acromioclavicular and coracoclavicular ligaments. *Journal of Shoulder and Elbow Surgery*, *32*(3), 526–532. https://doi.org/10.1016/j.jse.2022.09.004

Gelman, A., Carlin, J. B., Stern, H. S., Dunson, D. B., Vehtari, A., & Rubin, D. B. (2013). *Bayesian Data Analysis* (3rd ed.). Chapman; Hall/CRC.

Goodine, T., Celik, H., Flores-Hernandez, C., D'Lima, D., & Hoenecke, H. (2022). Combination of Surgical Techniques Restores Multidirectional Biomechanical Stability of Acromioclavicular Joint. *Arthroscopy - Journal of Arthroscopic and Related Surgery*, *38*(6), 1774–1783. https://doi.org/10.1016/j.arthro.2021.11.051

Hills-Meyer, P., & Stamm, J. (2019, May). *Anatomy and Physiology*. OpenStax. http://cnx.org/contents/14fb4ad7-39a1-4eee-ab6e-3ef2482e3e22@15.5

Hoffman, M. D., & Gelman, A. (2014). The No-U-Turn Sampler: Adaptively Setting Path Lengths in Hamiltonian Monte Carlo. *Journal of Machine Learning Research*, *15*, 1593–1623. http://mcmc-jags.sourceforge.net

Insua, D., Ruggeri, F., & Wiper, M. (2012, May). *Bayesian Analysis of Stochastic Process Models* (1st ed., Vol. 970). John Wiley & Sons.

Iraeus, J. (2026, January). TME196 - Dynamic FE and mathematical models 2026.

Iraues, J., John, J., Klug, C., & Kranjec, M. (2025, September). About VIVA+. VIVA+ Human Body Models. https://vivaplus.readthedocs.io/en/latest/about/

John, J., Klug, C., Kranjec, M., Svenning, E., & Iraeus, J. (2022). Hello, world! VIVA+: A human body model lineup to evaluate sex-differences in crash protection. *Frontiers in Bioengineering and Biotechnology*, *10*. https://doi.org/10.3389/fbioe.2022.918904

Jolliffe, I. T., & Cadima, J. (2016). Principal component analysis: a review and recent developments. *Philosophical transactions. Series A, Mathematical, physical, and engineering sciences*, *374*(2065). https://doi.org/10.1098/rsta.2015.0202

Kiel, J., Ponnarasu, S., & Kaiser, K. (2023, August). *Sternoclavicular Joint Injury*. StatPearls Publishing. http://www.ncbi.nlm.nih.gov/pubmed/18539660%20http://www.pubmedcentral.nih.gov/articlerender.fcgi?artid=PMC5622535

Kiel, J., Taqi, M., & Kaiser, K. (2022, September). *Acromioclavicular Joint Injury*. StatPearls Publishing. http://www.pubmedcentral.nih.gov/articlerender.fcgi?artid=PMC6129955

Koh, S.-W., Cavanaugh, J. M., Leach, J. P., & Rouhana, S. W. (2004). Mechanical Properties of the Shoulder Ligaments under Dynamic Loading. *Stapp Car Crash Journal*, *48*, 125–153.

Kranjec, M. (2024, October). VIVA+ Finite Element Model Validation Data: Shoulder Impact (Compigne 2004). https://openvt.eu/fem/viva/vivaplus-validation/-/blob/main/catalog/Compigne-2004-Shoulder-impact/data/processed/2024-10-29/dyna/6-0_50F/Dynasaur_output.csv?ref_type=heads

Krefeld, W. J., & Bowman, W. G. (2020, August). Young's modulus. AccessScience. Retrieved March 22. https://doi.org/10.1036/1097-8542.753700

Leyland AH, G. P. (2020). What Is Multilevel Modelling? In *Multilevel modelling for public health and health services research: Health in context*.

Livermore Software Technology. (2020). Ansys LS-DYNA Keyword User's Manual Volume II Material Models. https://www.dynasupport.com/manuals/ls-dyna-manuals/ls-dyna_manual_volume_ii_r12.pdf/view

Martin, O., Fonnesbeck, C., & Wiecki, T. (2024). *Bayesian analysis with Python : a practical guide to probabilistic modeling* (3rd ed.). Packt Publishing.

Morikawa, D., Huleatt, J. B., Muench, L. N., Kia, C., Berthold, D. P., Cote, M. P., Obopilwe, E., Kelolli, D., Scheiderer, B., & Mazzocca, A. D. (2020). Posterior Rotational and Translational Stability in Acromioclavicular Ligament Complex Reconstruction: A Comparative Biomechanical Analysis in Cadaveric Specimens. *American Journal of Sports Medicine*, *48*(10), 2525–2533. https://doi.org/10.1177/0363546520939882

Morita, N. (2021). *Finite Element Programming in Nonlinear Geomechanics and Transient Flow*. Gulf Professional Publishing. https://doi.org/10.1016/C2021-0-00098-5

Negri, J., Malavolta, E., Assunção, J., Gracitelli, M., Pereira, C., Bolliger Neto, R., Croci, A., & Ferreira Neto, A. (2014). Assessment of the function and resistance of sternoclavicular ligaments: A biomechanical study in cadavers. *Orthopaedics & Traumatology: Surgery & Research*, *100*(7), 727–731. https://doi.org/10.1016/j.otsr.2014.07.011

Reddy, J. N. (2019). *Introduction to the finite element method* (4th ed.). McGraw Hill Education.

ScienceFacts. (2025, June). Poisson's ratio. https://www.sciencefacts.net/poissons-ratio.html

Spencer, E. E., & Kuhn, J. E. (2004). Biomechanical Analysis of Reconstructions for Sternoclavicular Joint Instability. *Journal of Bone and Joint Surgery*, *86*, 98–105.

Sun, W., Jin, J. H., Reed, M. P., Gayzik, F. S., Danelson, K. A., Bass, C. R., Zhang, J. Y., & Rupp, J. D. (2016). A method for developing biomechanical response corridors based on principal component analysis. *Journal of biomechanics*, *49*(14), 3208–3215. https://doi.org/10.1016/j.jbiomech.2016.07.034

Swedish Environmental Research Institute. (n.d.). Vision Zero- Reducing Roas Traffic Casualties and Injuries. Smart City Sweden. Retrieved May 12. https://smartcitysweden.com/best-practice/408/vision-zero-reducing-road-traffic-casualties-and-injuries/

The Engineering ToolBox. (2008). Poisson's Ratio - Definiftion, Values for Materials, and Applications. Retrieved March 25. https://www.engineeringtoolbox.com/poissons-ratio-d_1224.html

Toyota Motor Corporation. (2021, January). Total Human Model for Safety (THUMS): Revolutionizing Crash Simulation to Support Safe Mobility for all. https://www.toyota.co.jp/thums/contents/pdf/Toyota_THUMS_History_English.pdf

World Health Organization. (2023). *Global status report on road safety 2023* (tech. rep.). https://iris.who.int/server/api/core/bitstreams/46275f9f-ef66-4892-8ddd-a496ef8c1b74/content

A

Appendix 1

A.1 Ramp up

Table A.1: Ramp-up function

Time	Value
0.00	0.0000000
0.05	0.0061555
0.10	0.0244703
0.15	0.0544936
0.20	0.0954861
0.25	0.1464384
0.30	0.2060961
0.35	0.2729903
0.40	0.3454739
0.45	0.4217622
0.50	0.4999768
0.55	0.5781921
0.60	0.6544821
0.65	0.7269684
0.70	0.7938664
0.75	0.8535288
0.80	0.9044867
0.85	0.9454854
0.90	0.9755154
0.95	0.9938373
1.00	1.0000000
100.00	1.0000000

Table A.2: Material properties used for sternum and clavicle potting in the Spencer (2004) AP test

Component	Material	ρ (kg/mm^3)	E (GPa)	ν
Sternum potting (inner)	PMMA	$1.18 \cdot 10^{-6}$	2	0.35
Sternum potting (outer)	Aluminum	$2.7 \cdot 10^{-6}$	70	0.33
Clavicle potting (inner)	PMMA	$1.18 \cdot 10^{-6}$	2	0.35
Clavicle potting (outer)	Polyvinylchloride	$1.4 \cdot 10^{-6}$	3	0.38

A.2 Material properties

A.3 PC Corridors

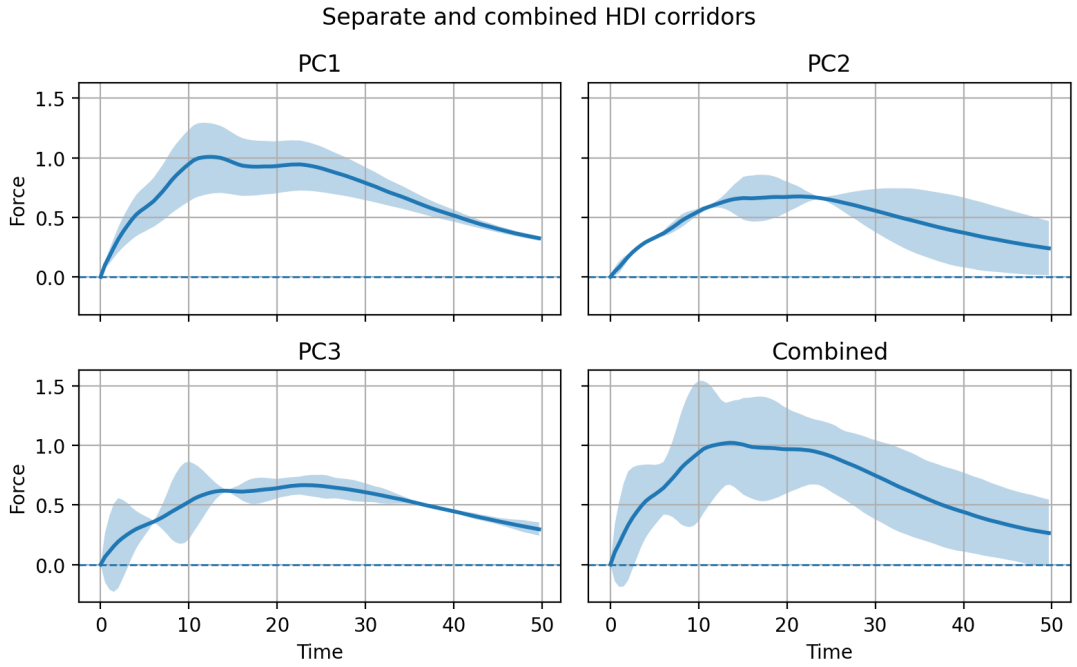

Figure A.1: Separate corridors for each PC.

Department of Mechanical Engineering
Chalmers University of Technology
Gothenburg, Sweden 2026
www.chalmers.se

CHALMERS